

DEVELOPMENT OF TRIPROPELLANT CFD DESIGN CODE

Contract No.: NAS8-40583

FINAL REPORT

Prepared for:

**National Aeronautics & Space Administration
George C. Marshall Space Flight Center
Marshall Space Flight Center, AL 35812**

Prepared by:

**Richard C. Farmer
Gary C. Cheng
Peter G. Anderson**

**SECA, Inc.
Suite 202
3313 Bob Wallace Avenue
Huntsville, AL 35805**

May, 1997

SUMMARY

A tripropellant CFD design code has been developed to predict the local mixing of multiple propellant streams as they are injected into a rocket motor. The tripropellant system of primary interest is $\text{GO}_2/\text{H}_2/\text{RP-1}$. The code utilizes real fluid properties to account for the mixing and finite-rate combustion processes which occur near an injector faceplate. Thus the analysis serves as a multi-phase homogeneous spray combustion model, which explicitly avoids the droplet tracking analysis that makes alternative analyses extremely slow to compute. Of course, simplification could have been affected by compromising the combustion description and emphasizing the droplet tracking. However, proper accounting of the combustion allows accurate gas-side temperature predictions which are essential for accurate wall heating analyses. The complex secondary flows which are predicted to occur near a faceplate cannot be quantitatively predicted by less accurate methodology. Since very few tripropellant injector experiments have been reported, the methodology has also been applied to bipropellant injectors to aid in its validation. Test cases have been simulated to describe an axisymmetric tripropellant coaxial injector and a 3-dimensional $\text{RP-1}/\text{LO}_2$ impinger injector system. The analysis has been shown to realistically describe such injector combustion flowfields, but further exercising of the code is necessary to accomplish its computational optimization. Since the details of the predicted combustor flowfields exceed the state-of-the-art capabilities to measure such flowfields, the code is also valuable to design meaningful future experiments by determining the critical location and type of measurements needed.

TABLE OF CONTENTS

SUMMARY	i
1.0 INTRODUCTION	1
2.0 METHODOLOGY	2
2.1 Real Fluids Version of FDNS	2
2.2 Fluid Properties	4
2.3 Combustion Kinetics	8
2.4 Radiation From Sooty Flames	8
3.0 INJECTOR ANALYSES	10
3.1 Global Analysis of the Fastrack Motor	10
3.2 GO_2/GH_2 Coaxial Injector	18
3.3 LO_2/GH_2 Coaxial Injector	27
3.4 Tripropellant Coaxial Injector	27
3.5 Fastrack Injector Configuration	32
4.0 CONCLUSIONS AND RECOMMENDATIONS	38
5.0 REFERENCES	39
APPENDIX A - RADIATION EFFECTS	A- 1
Radiative Properties	A- 1
Homogeneous Gray Model	A- 2
Homogeneous Nongray Model	A- 2
Non-Homogeneous Nongray Model	A-11
Solution of the Radiative Transfer Equation	A-11
Coupled Radiative Transfer Equation Solutions	A-13
Nomenclature for Appendix A	A-15
References for Appendix A	A-16

DEVELOPMENT OF TRIPROPELLANT CFD DESIGN CODE

1.0 INTRODUCTION

SECA, Inc. has developed a CFD design code to describe the operation of a tripropellant injector system, which, for example, utilizes both RP-1 and H_2 as fuels. This model is sufficiently general to define the mixing characteristics of several injector concepts. Future engine designs may be devised with the code developed in this investigation. The code provides the local mixture ratio and state of the propellants near the injector face so that the remainder of the combustor flow can be calculated with conventional multi-species gas-only CFD codes. It is anticipated that laboratory test data will become available to validate the CFD injector model, although adequate data do not currently exist.

The objective of developing an advanced tripropellant CFD design code is to provide an analytical method to predict the local mixing of the multiple propellant streams as they are injected into the motor. This analysis must be described with a computer code which is sufficiently fast to provide very detailed predictions and structured to be used as a submodel in a general three-dimensional CFD simulation of the entire motor operation. It is recognized that other spray combustion models have been and are being developed, but such models have not matured to the point that efficient rocket performance and heating analyses can be made for practical rocket motor designs. Extensive data bases and much experience are available for designing bipropellant rocket motor injectors, but such valuable information is not available for tripropellant and advanced bipropellant injectors. Furthermore, the new CFD design code can be used to reduce the large number of costly experimental injector studies which would otherwise be required to design future rocket motors.

To describe tripropellant combustors, real fluid properties representing both sub- and super-critical conditions for RP-1, H_2 , and O_2 must be used. A combustion kinetics model for RP-1 including soot formation and oxidation was developed. Radiation from sooty combustion gases is important and was assessed, but, due to a reduction in program funding, was not included in the final CFD model. To treat fluids in arbitrary states, the pressure correction step in the FDNS CFD code was completely changed from the method which has been used for ideal gases and incompressible liquids. The tripropellant CFD design code resulting from this development is termed the Finite Difference Navier-Stokes - Real Fluids Version (FDNS-RFV) code.

The tripropellant design code produced from this research meets the objectives of the proposed study and may be termed a homogeneous spray combustion code. Since the mixed gas/liquid flowfield is analyzed without identifying and tracking drops, the gas and liquid are always assumed to be in thermal equilibrium. This assumption greatly simplifies the calculation while still approximating the multi-phase flow near the injector face. The limitations and alternatives to using this assumption are discussed in this report. Both shear coaxial and impinging doublet injectors were simulated with the code as demonstration cases.

2.0 METHODOLOGY

During the course of the Space Shuttle Main Engine (SSME) and the Fastrack engine design processes, severe erosion problems on the liner wall near the injector face have occurred. Study and understanding of the spray combustion flows have posed a great challenge to the injector, and hence, the rocket engine design. The effect of the spray vaporization is also important in analyzing the internal ballistics of rocket motors. Though extensive experimental studies can help designers/researchers understand and analyze the flow characteristics, building various injector/motor hardware can be very costly. Hence, an efficient CFD spray combustion code can improve the rocket engine design and reduce the cost of hardware. The objective of the present work is to develop an efficient CFD design tool to simulate real fluid injector flowfields for the liquid and hybrid rocket engines. Lately, CFD methodology has improved to the point that numerical analyses of turbulent, reacting flows provide practical design models for combustion devices. However, multi-phase (liquid-spray) combustion CFD models are still under development. The main reason is that not many experimental studies for spray combustion flows have been conducted, and, unfortunately, most of those tests did not provide detailed flow data. Hence, the underlying physics is still not well understood, and this shortcoming is reflected in the available CFD spray combustion models. Due to the importance of the benchmark test data for spray combustion flows, NASA Marshall Space Flight Center funded Pennsylvania State University to conduct experimental tests to provide flowfield measurements of the gas/liquid coaxial injector¹⁻². The availability of such data allow the present homogeneous CFD spray combustion model to be benchmarked to the extent that sufficient measurements were made. Deleting the droplet tracking simplifies the CFD code to the point where meaningful 3-D flowfield simulations and design studies can be made.

Tripellant injection may be accomplished with elements comprised of like- or unlike-doublets, triplets, or other variations of coaxial injectors. All of these configurations require that three-dimensional CFD analyses be performed to describe the initial mixing of a single injector element. The entire injector assembly must then be described with an ensemble of such injectors or with alternative methodology.

The complete combustor/preburner tripellant CFD design code (FDNS-RFV) will require: (1) definition of the inlet boundary conditions to each representative injector element, as obtained from a model of the feed system such as that provided by SECA's porosity model for the SSME main combustion chamber³, (2) the CFD analysis of each representative injector element (the number of representative elements should be small, for a given motor design); and finally (3) the use of the injector model results as boundary conditions for a CFD simulation of the entire motor and nozzle flow. The injector element analysis shall be accomplished with a CFD calculation. The injector element analyses shall provide streamtube bundles to initiate a CFD simulation of the entire combustor. Both the injector element analyses and the entire motor analysis can be used to determine local wall heating effects.

2.1 Real Fluids Version of FDNS (FDNS-RFV)

The framework of the CFD model is an elliptic, Finite Difference Navier-Stokes (FDNS) flow solver⁴⁻⁵, which employs a predictor plus multi-corrector pressure-based solution algorithm

so that both compressible and incompressible flow problems can be analyzed. High order upwind, total variation diminishing (TVD), or central difference schemes plus adaptive second-order and fourth-order dissipation terms are used to approximate the convection terms of the transport equations such that computed supersonic flows through a shock regime will be stabilized. Second-order central differencing schemes are used for the viscous and source terms of the governing equations. Vectorized point implicit, conjugate gradient, and generalized minimal residual matrix solvers⁶ (GMRES) are optionally employed to insure a stable, accurate, and fast convergence rate. Multi-block, multi-zone options are included in the FDNS code so that problems with complex geometries can be analyzed efficiently. An extended k- ϵ turbulence model with a modified near-wall boundary treatment⁷ is utilized in the code for turbulent flow computations. In this approach, the profile of the non-dimensionalized velocity u^+ is formulated based on the velocity profile suggested by Liakopoulos⁸. This velocity profile provides a smooth transition between logarithmic law of the wall and linear viscous sublayer variations. In addition, a modified wall function treatment⁹, which is suitable for compressible flows by accounting for the aerodynamic heating effects, had previously been incorporated in FDNS to provide appropriate heat transfer calculations near wall boundaries. To simulate spray combustion flows, several additional submodels, as described in subsequent paragraphs, were developed and incorporated into the FDNS code under the Phase II SBIR investigation¹⁰ which this Phase III study is derived from. The Phase II¹⁰ progress reports also provide more detail for the methodology reported herein.

In order to analyze the effect of phase changes in the spray combustion flows, real-fluid thermal and caloric equations of state were developed¹⁰. Interfacial heat and mass transfer effects were neglected for the very high pressure (near or above critical pressure) in existing rocket engine combustion chambers. The HBMS equations of state^{11,12} were selected for this purpose. These equations are:

$$\frac{P}{P_c} = \sum_{j=1}^4 T_r^{j-2} \sum_{i=1}^6 B_{ij} \rho_r^{i-2} ; \quad T_r = \frac{T}{T_c} ; \quad \rho_r = \frac{\rho}{\rho_c} \quad (1)$$

$$\frac{H - H_0}{RT} = Z_c \int_0^{\rho_r} \left[\frac{P}{T_r} - \left(\frac{\partial P}{\partial T_r} \right)_{\rho_r} \right] \rho_r^{-2} d\rho_r + Z_c \frac{P}{\rho_r T_r} - 1 \quad (2)$$

where P_c , T_c , ρ_c , and Z_c are the pressure, temperature, density, and compressibility at the critical condition. B_{ij} are the coefficients of the thermal property polynomial for a given species. H and H_0 are the real-fluid enthalpy and ideal-gas enthalpy for a given species, and R is the gas constant. These equations are not only of sufficiently high order that properties are accurately predicted for a wide range of conditions, but component submodels may be easily modified. In this instance, the vapor pressure curve and the liquid phase density correlations were improved over the original HBMS formulation. Multicomponent mixtures were treated by adding partial specific volumes or pressure. The partial volume methodology is essential to provide accurate and robust predictions when a small amount of multi-component vapor and a large amount of liquid, or vice versa, are present at the same location. The properties routines also include correlations for the transport properties. Furthermore, this real-fluid property submodel can be

ported into other CFD code, or used as a stand alone program.

Most of the pressure-based methods are constructed based on the perfect gas law, which is no longer valid in simulating the spray combustion flows. In the present model, flow mixture density is calculated in two steps. In the predictor step, a constant pressure procedure is employed to solve flow velocity components, mixture energy and species concentrations, and then the flow mixture density and temperature are calculated from the real-fluid model. Like other pressure-based methodology, a correlation between pressure and density is used to convert the continuity equation to the pressure-correction equation as the corrector step. However, the perfect gas law can not be used as the correlation. In the present model, a constant-temperature derivative is used to correlate the pressure change and the density:

$$\rho' = P' \left[\frac{d\rho}{dP} \right]_T = P' \gamma \left[\frac{d\rho}{dP} \right]_T = \beta_p P' \quad (3)$$

$$\text{where for the perfect gas: } \beta_p = \frac{1}{RT} \quad (4)$$

$$\text{and for the real-fluid model: } \beta_p = \frac{\gamma}{a^2} \quad (5)$$

where γ , R and a are the specific heat, gas constant and sonic speed of the flow mixture, respectively. Hence, the pressure-correction equation can be derived from the continuity equation based on the above correlation, and can be written as

$$\frac{\beta_p P'}{\Delta t} + \nabla \cdot (V \beta_p P') - \nabla \cdot (\rho^* D_p \nabla P') = -\nabla \cdot (\rho^* V) - \frac{\rho^* - \rho^n}{\Delta t} \quad (6)$$

where D_p is the matrix coefficient of the momentum equations, and the superscripts of $*$ and n denote the values at the intermediate and previous time steps.

2.2 Fluid Properties

Methods for estimating real fluid properties of $\text{LO}_2/\text{RP-1}/\text{H}_2$ mixtures and their combustion products have been developed^{10,13} and included in the FDNS-RFV code. The properties of a RP-1 surrogate fuel are presented in Table 1. The Core Labs report on RP-1¹⁰ approximated the constituents to be about 42% liquid volume of paraffins, 25% monocycloparaffins, 24% di- and tri-cycloparaffins, 3% benzenes and 6% naphthalenes. Examination of the constituents revealed about 12% liquid volume of molecules with 10 carbon atoms (C10's), 13% C11's, 29% C12's, 25% C13's, 11% C14's and the rest either larger or smaller. The surrogate fuel was designed to incorporate these breakdowns into the formulation.

In order to simplify the surrogate model, the carbon breakdown was reduced to 20%

Table 1. Surrogates for RP-1

Species	Type	Formula	Vol %	Den	Mole Fr
n-UNDECANE	Paraffin	C11H24	4.70	.781	.05013
DODECANE	Paraffin	C12H26	6.00	.791	.05948
n-TRIDECANE	Paraffin	C13H28	18.80	.819	.17828
n-TETRADECANE	Paraffin	C14H30	12.50	.761	.10235
n-HEXYLCYCLOPENTANE	Monocyclic Paraffin	C11H22	2.70	.782	.02921
n-HEPTYLCYCLOPENTANE	Monocyclic Paraffin	C12H24	3.60	.782	.03570
n-OCTYLCYCLOPENTANE	Monocyclic Paraffin	C13H26	11.20	.796	.10437
n-NONYLCYCLOPENTANE	Monocyclic Paraffin	C14H28	7.50	.803	.06547
BICYCLOPARAFFIN1	Polycyclic Paraffin	C11H20	11.30	.852	.13496
BICYCLOPARAFFIN2	Polycyclic Paraffin	C12H22	14.70	.819	.15453
PENTAMETHYLBENZENE	Mononuclear Aromatic	C11H16	1.30	.806	.01509
HEXAMETHYLBENZENE	Mononuclear Aromatic	C12H18	1.70	.786	.01758
DIMETHYLNAPHTHALENE	Dinuclear Aromatic	C12H12	4.00	.967	.05285
Formula			C12.39H24.15		
H/C			1.9492		
Molecular Weight			173.1453		
Liquid Density			.8111 gm/cc		
Breakdown of Number of Carbon Atoms per Molecule					
Fraction of LV of C11s (.20)			20.0000		
Fraction of LV of C12s (.30)			30.0000		
Fraction of LV of C13s (.30)			30.0000		
Fraction of LV of C14s (.20)			20.0000		
Breakdown of Liquid Volume by Type					
Paraffins (.42)			42.0000		
Monocyclic Paraffins (.25)			25.0000		
Polycyclic Paraffins (.24)			26.0000		
Mononuclear aromatics (.03)			3.0000		
Dinuclear aromatics (.06)			4.0000		
Stoichiometric Products:					
Moles of O ₂ burned			18.426		
Moles of CO ₂ formed			12.389		
Moles of H ₂ O formed			12.075		
Heat of Formation of Surrogates			-.56940E+02 kcal/mol		
			-.32886E+02 kcal/100gm		
Heat of Formation of Products			-.18631E+04 kcal/mol		
			-.10760E+04 kcal/100gm		
Heat of Combustion			-.18061E+04 kcal/mol		
			-.10431E+04 kcal/100gm		

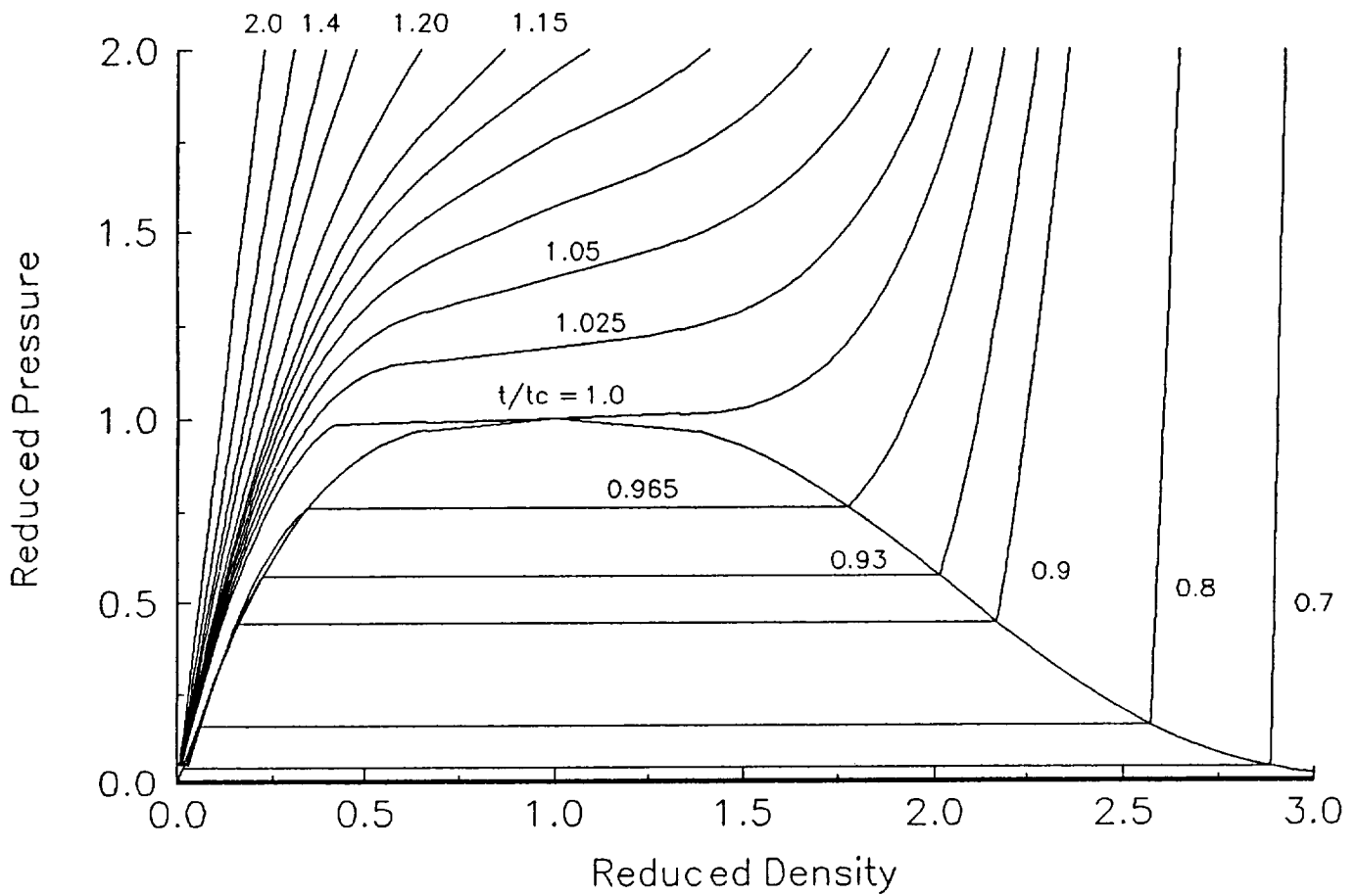
C11's, 30% C12's, 30% C13's and 20% C14's. Eighteen candidate constituents were identified which satisfied both Core Lab breakdowns. Various liquid volume fractions of each were analyzed and compared to estimated RP-1 molecular weight (175), hydrogen to carbon ratio ($H/C = 1.95$) and liquid density (0.83 grams/cc). A reasonable value of H/C was unattainable due to the low H/C 's for aromatics. Since the reported percentage (9%) of aromatics was higher than reported by other sources, and since complex dinuclear aromatics (naphthalenes) are often indistinguishable from polycyclic paraffins, the naphthalenes percentage was reduced by 2% and the polycyclic paraffin percentage was increased by 2%. This resulted in an H/C close to 1.95. These considerations are reflected in the surrogate shown in Table 2.

Table 2. Critical Properties for RP-1 Surrogate					
Species	Mol Fr.	Pc(bar)	Tc(°K)	Vc(gmol/cc)	Zc
n-UNDECANE	.05013	19.70	638.80	647.05	.240
DODECANE	.05948	18.20	658.20	694.58	.231
n-TRIDECANE	.17828	17.20	676.00	784.25	.240
n-TETRADECANE	.10235	14.40	693.00	920.29	.230
n-HEXYLCYCLOPENTANE	.02921	21.30	660.10	590.05	.229
n-HEPTYLCYCLOPENTANE	.03570	19.40	679.00	689.67	.237
n-OCTYLCYCLOPENTANE	.10437	17.90	694.00	744.64	.231
n-NONYLCYCLOPENTANE	.06547	16.50	710.50	805.54	.225
BICYCLOPARAFFIN1	.13496	27.79	712.20	539.09	.253
BICYCLOPARAFFIN2	.15453	24.36	721.80	593.72	.241
PENTAMETHYLBENZENE	.01509	24.85	719.00	541.27	.225
HEXAMETHYLBENZENE	.01758	22.40	758.00	607.72	.216
DIMETHYLNAPHTHALENE	.05285	31.09	771.00	517.53	.251
Mixture Critical Temperature (K)			692.776		
Mixture Critical Pressure (bar)			19.974		
Mixture Critical Volume (cc/gmol)			646.093		
Mixture Critical Zc			.224		

The true critical properties for the RP-1 surrogate fuel were calculated using Gibbs method¹³. Unknown saturated liquid volumes of the constituents were estimated using the method of Gunn and Yamada¹⁴. Unknown critical properties were estimated using the group contribution method of Joback¹⁵. As before, Gibbs method resulted in a high value for the mixture critical volume. The literature¹⁴⁻¹⁶ suggest using the resultant critical pressure and temperature but not the critical volume when Gibbs method is employed with cubic equations of state. An alternative was to use the method of Chueh and Prausnitz¹⁴ to estimate critical volume. This method utilizes an interaction parameter which varies depending on whether the constituent is a paraffin, cycloparaffin, aromatic, etc. These interaction parameters cause the critical volume to vary wildly, hence care must be used in evaluating them. For the complex molecules, such as n-nonylcyclopentane or hexamethylbenzene, more than one category may be applicable. These methods were utilized and the interaction parameters adjusted until a reasonable value for the critical volume was obtained. The results are presented in Table 2. A plot of the resulting thermal equation of state is shown in Figure 1.

Figure 1

Pressure and Density Along Isotherms
RP-1 Comprised of 13 Surrogates



2.3 Combustion Kinetics

Combustion kinetics rates for H_2 /RP-1 at high pressures are very fast except possibly for the formation and oxidation of soot and for the pyrolysis of RP-1 constituents. If local chemical equilibrium were assumed, ignition delays upon injection could not be predicted, no soot would be formed if any oxygen were present, and all large molecular species in the RP-1 would be immediately pyrolyzed. The RP-1 contains a mixture of so many species that they cannot be rigorously identified. Kinetics models for RP-1 oxidation that treat the hydrocarbons as either large aromatics, large aliphatics, or small two-carbon fragments are desirable, but such models are too complex for direct use in a CFD code. The species which comprise RP-1 change from lot-to-lot of the fuel, but these composition changes are unknown, therefore the one surrogate fuel characterization was used. One global pyrolysis/partial-oxidation step for the surrogate fuel was used as the RP-1 kinetics model. The rate used for this global step is given in Table 3. The combustion is completed by a wet CO equilibrium model. This RP-1 kinetics model accounts for the large amounts of H_2 which would be present in a tripropellant with the equilibrium H_2/O_2 steps in the wet CO reactions. H_2/O_2 combustion for gaseous O_2 is modeled as an equilibrium process. For the LO_2/H_2 cases analyzed in this report, the global reaction shown in Table 4 was used. The approximation introduced with this global model is that the distribution of combustion products is evaluated for equilibrium combustion at one mixture ratio. If the stoichiometric coefficients were expressed as a function of local mixture ratio, the global equation simulation could be made quite accurately. However, as it was used, this model is an approximation which is considerably better than assuming complete combustion and is computationally efficient.

2.4 Radiation From Sooty Flames

RP-1 and hybrid fuels tend to form soot during the combustion process. Soot, as well as the gases CO_2 , H_2O , and CO , produce significant thermal radiation. Since the soot particles are expected to be small, the soot radiation is continuum and is exchanged by emission and absorption only, as is the radiation for the gases. However, gaseous radiation is strongly and discontinuously wavelength dependent. To predict radiation in combustion devices, three factors must be considered: (1) radiation properties for the optically active species, (2) the method of calculating the radiative exchange, and (3) the accuracy of the concentration predictions of the radiating gas species and particles. The essential elements which define these factors are presented in Appendix A. No attempt has been made to compromise the radiation analysis presented in Appendix A solely for computational expediency.

The critical issue is the accurate prediction of soot and liquid masses and drops. Absolutely no data to indicate the magnitude of the radiation shielding effects of liquid particles in the vicinity of the injector face-plate are available. Gaseous species must also be predicted, but these predictions are both more accurate and less critical since gases account for less of the radiation. The flowfield analyses described in this report are useful for making such predictions; however, identification of typical combustion systems and validation data must be accomplished. The CFD solutions are too cumbersome to yield the necessary flowfield data for an indiscriminate parametric investigation of combustors. Definitive experiments to define radiation in tripropellant rocket combustion devices are non-existent. Since soot predictions and their

verification are the final result of tripropellant flowfield analyses and since this investigation was foreshortened because of funding reductions, the radiation methodology described in Appendix A was not used to make radiation predictions for tripropellant systems. The radiation aspects of tripropellant systems should be revisited when (and if) more firm design concepts are established.

Table 3. Combustion Kinetics Models for RP-1/O₂

<p>RP-1 + 6.195 O₂ → 12.39 CO + 12.075 H₂ Rate = $AT^B \exp\{-E/RT\} [\text{RP-1}]^{0.5} [\text{O}_2]^{1.0}$ A = 4.4963x10⁹, B = 1, E/R = 2.679x10⁴</p>			
<p>RP-1 → 12.39 C_s + 12.075 H₂ Rate = $A \exp\{-25(1-T/T_0)^2\} [\text{RP-1}]^{1.43} [\text{O}_2 + \epsilon]^{-0.5}$ A = 0.5, T₀ = 1700°K, $\epsilon = 0.001\rho/M_{\text{O}_2}$ g-mole/cm³</p>			
<p>C_s + 0.5 O₂ → CO</p> $\text{Rate} = \frac{6 M_{w_s} R_u T}{\rho_s D_s} \left[\frac{K_1 \psi}{1 + K_4 P_{\text{O}_2}} + K_2 (1 - \psi) \right] [C_s] [O_2]$ <p>where $\psi = \left[1 + \frac{P_{\text{O}_2} K_3}{K_2} \right]^{-1}$; and $K_i = A_i e^{\frac{-E_i}{RT}}$, i = 1 → 4</p> <p> A₁ = 20, E₁/R = 1.509x10⁴ A₂ = 4.46x10⁻³, E₂/R = 7.6497x10³ A₃ = 1.51x10⁵, E₃/R = 4.8817x10⁴ A₄ = 21.3, E₄/R = -2.0634x10³ R_u = 82.06 atm·cm³/g-mole·°K ρ_s (density of soot) = 1.86 g/cm³ D_s (particle diameter of soot) = 40 nm (assumed value) M_{w_s} (molecular weight of soot) = 12 g/g-mole P_{O₂} (partial pressure of O₂, in atm) = P·N_{O₂} (N_{O₂}: mole fraction of O₂) </p>			

Table 4. Combustion Global Kinetic Model for H₂/O₂

Reaction	A	B	E/R
1.827 H ₂ + O ₂ → 1.552 H ₂ O + 0.094 O + 0.196 H + 0.354 OH	3.1000E22	0	2.4070E4

3.0 APPLICATIONS TO INJECTOR DESIGN

At the inception of this investigation, strong consideration was being given to the use of tripropellant rocket motors which utilized H_2 , RP-1, and O_2 . Both impinging and coaxial elements were being evaluated. Subsequent NASA programs dropped the tripropellant concept. The only tripropellant injector design which has been experimentally investigated was the effervescent H_2 /RP-1 coaxial injector¹⁷. Therefore, due to the lack of validation data, several bipropellant injectors of the type used in the Fastrack motor and bipropellant coaxial elements, as well as, the aforementioned coaxial tripropellant injector were simulated to evaluate the tripropellant CFD design code. The results of these simulations are reported in this section.

3.1 The Entire Fastrack Motor

To initiate the study of clustering injector elements to represent an entire combustor, a series of a 2-D axisymmetric numerical global simulations of the Fastrack test motor were conducted. The major goal of this study was to determine the temperature along the motor wall, in order that wall heating could be subsequently evaluated. The motor configuration is shown in Figure 2. The flow conditions which were used to parametrically represent the injector flow are shown in Tables 5-7. Uniform flow of combustion gas through most of the injector and center flow and film cooling flow of RP-1 were used to represent the injector configuration. At first, an ideal gas model was employed to simulate RP-1 and combustion gas. A large gap for the center fuel flow and outer film cooling flow was used as shown in Table 5, to compensate for the low density RP-1 vapor. For the ideal gas model, two numerical calculations were conducted, one was with frozen chemistry and the other with finite-rate chemistry. The results shown in Fig. 3, indicate that the difference is very small because the major part of the flow is in the chemical equilibrium and is unaffected by the small amount of fuel which flows through the center and outer coolant streams. Therefore, the frozen chemistry at equilibrium chamber conditions was chosen for further study. Figure 4 shows the results of the ideal gas model with frozen chemistry simulation.

In order to study the effect of a liquid phase for the center fuel and the outer coolant fuel flow, the real fluids model was employed to simulate these two streams, as opposed to the ideal gas in the previous calculation. Initially, the film coolant was assumed to occupy the space between a point midway radially between the film coolant holes and the outer row of primary fuel holes. The small-gap case assumed that the film coolant was injected through an area defined by a ring of thickness equal to the gap between the film coolant holes and the wall. As a result, the predicted wall temperature is much lower than in the previous case and is thought to be a better simulation of actual conditions.

Two different mixing models, the extended $k-\epsilon$ model with and without a temperature correction were used to study the effect of compressibility on the species mixing and thus on the nozzle wall temperature. The temperature correction model modifies the source term S_ϵ in the ϵ equation as

Figure 2
SKETCH OF FAST TRACK NOZZLE GEOMETRY

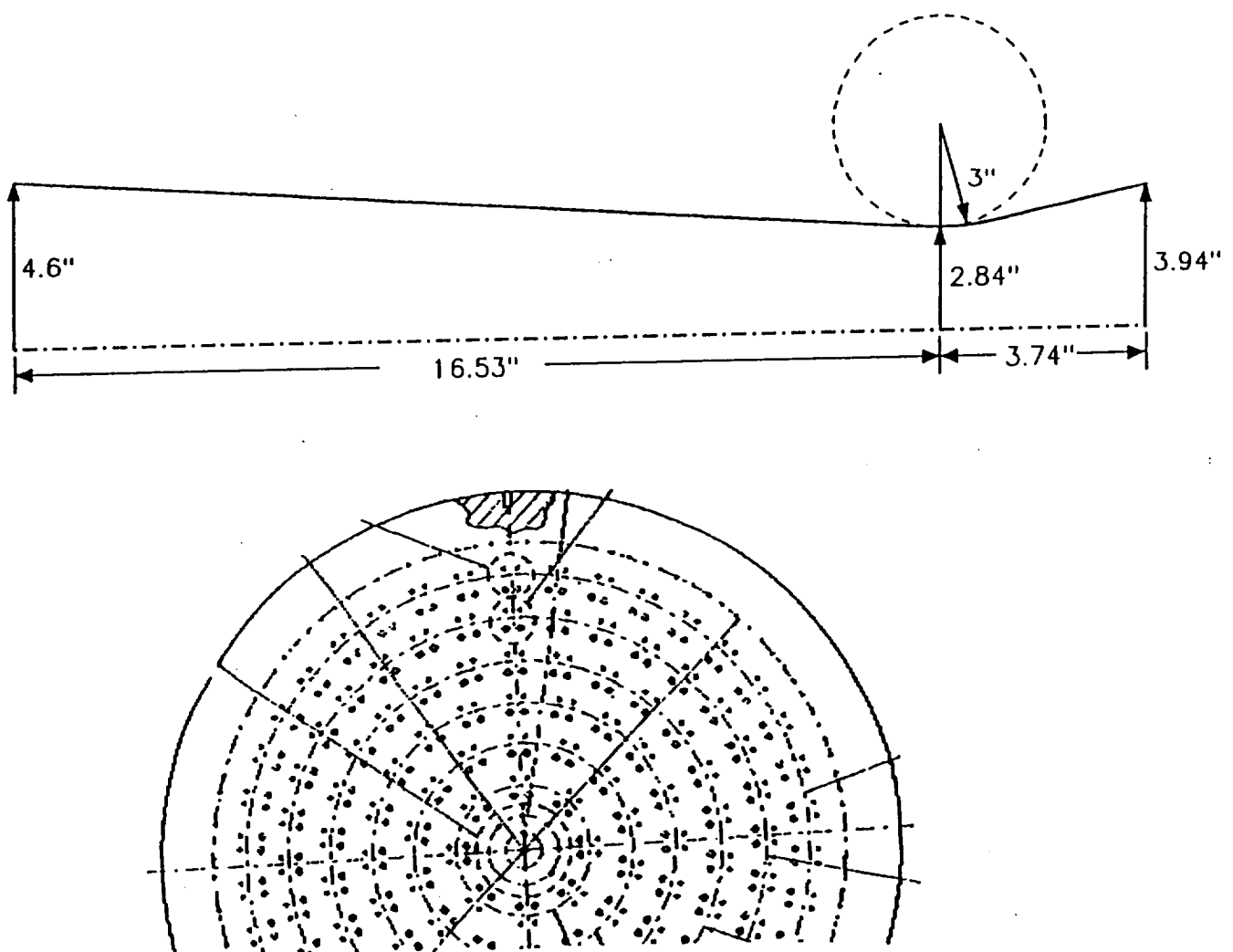


**Table 5. INLET CONDITIONS FOR FAST TRACK NOZZLE SIMULATION
(IDEAL GAS, LARGE GAP)**

	Inner Fuel Region	Hot Gas Mixture	Outer Fuel Region
RP-1 flow rate	0.76678 lb/sec	21.16322 lb/sec	3.32 lb/sec
O ₂ flow rate	0	55.78 lb/sec	0
Starting/Ending radial location	0/0.65"	0.65"/4.323"	4.323"/4.6"
Temperature	532 °R	6714 °R	532 °R
Density	15.457 lb/ft ³	0.16457 lb/ft ³	15.457 lb/ft ³
Axial Velocity	5.382 ft/sec	1173.25 ft/sec	3.983 ft/sec

**Table 6. INLET CONDITIONS FOR FAST TRACK NOZZLE SIMULATION
(REAL FLUID MODEL, LARGE GAP)**

	Inner Fuel Region	Hot Gas Mixture	Outer Fuel Region
RP-1 flow rate	0.76678 lb/sec	21.16322 lb/sec	3.32 lb/sec
O ₂ flow rate	0	55.78 lb/sec	0
Starting/Ending radial location	0/0.65"	0.65"/4.323"	4.323"/4.6"
Temperature	532 °R	6714 °R	532 °R
Density	54.04 lb/ft ³	0.16457 lb/ft ³	54.04 lb/ft ³
Axial Velocity	1.539 ft/sec	1173.25 ft/sec	1.139 ft/sec

**Table 7. INLET CONDITIONS FOR FAST TRACK NOZZLE SIMULATION
(REAL FLUID MODEL, SMALL GAP)**

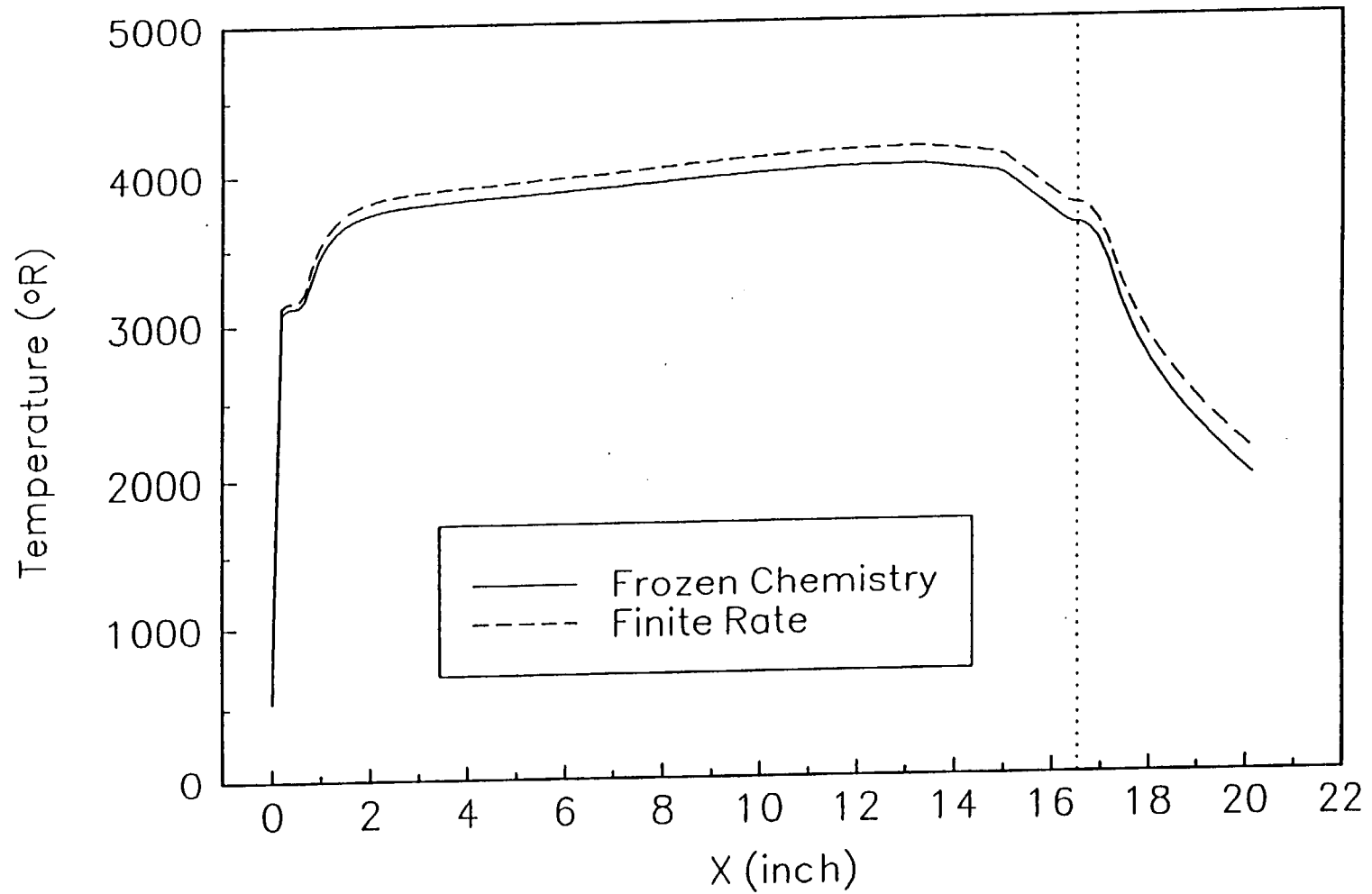
	Inner Fuel Region	Hot Gas Mixture	Outer Fuel Region
RP-1 flow rate	0.76678 lb/sec	21.16322 lb/sec	3.32 lb/sec
O ₂ flow rate	0	55.78 lb/sec	0
Starting/Ending radial location	0/0.45"	0.45"/4.5"	4.5"/4.6"
Temperature	532 °R	6714 °R	532 °R
Density	54.04 lb/ft ³	0.16457 lb/ft ³	54.04 lb/ft ³
Axial Velocity	3.212 ft/sec	1068.99 ft/sec	3.095 ft/sec

**Table 8. NUMERICAL RESULTS OF THE NOZZLE EFFICIENCY
AND WALL TEMPERATURE FOR VARIOUS MODELS**

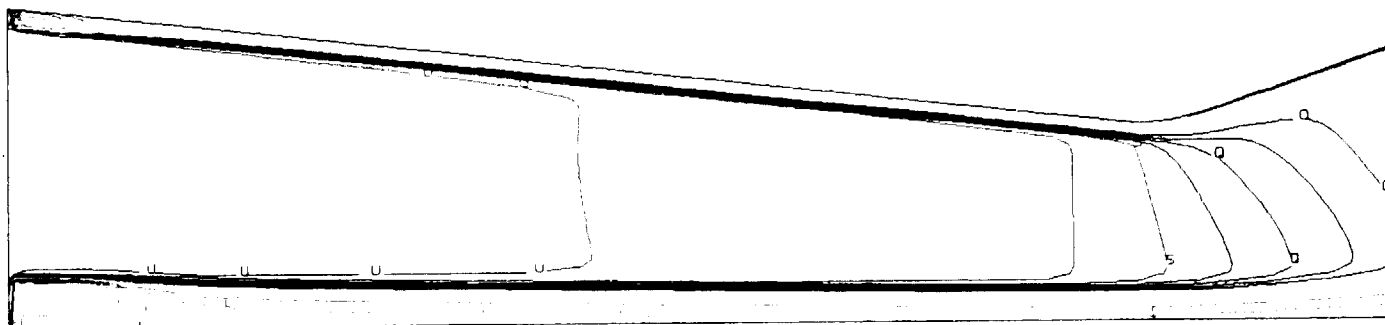
		C^*_{static} (ft/s)	C^*_{total} (ft/s)	η_c	T_{throat} (°R)
CEC Calculation		---	5987	---	5987
Gas RP-1 (large gap)	frozen chemistry	5474	5663	0.946	3618
	finite rate	5505	5705	0.953	3750
Liquid RP-1 (large gap)	extended k- ϵ	5300	5483	0.916	4158
	T-corrected k- ϵ	5275	5457	0.911	3742
Liquid RP-1 (small gap)	extended k- ϵ	5340	5555	0.928	4334
	T-corrected k- ϵ	5347	5563	0.929	3550

Figure 3

TEMPERATURE DISTRIBUTION ALONG NOZZLE WALL (Ideal Gas for RP-1)



Temperature (deg K, gas RP-1/hot gas mixing)



XMIN -5 0674E-01

XMAX 2 0776E+01

YMIN -6 5681E+00

YMAX 1 1168E+01

FMIN 2 9556E+02

FMAX 3 7342E+03

DELF 1 7009E+02

CONTOUR LEVELS

ID VALUES

A 2 9840E+02

B 4 6850E+02

C 1 3100E+02

D 1 4000E+02

E 1 5000E+02

F 1 6000E+02

Q 2 6797E+03

P 2 8498E+03

Q 3 0198E+03

R 3 1899E+03

S 3 3E00E+03

T 3 5301E+03

U 3 7002E+03

Figure 4

$$S_e = \rho \left[C_1 Pr \frac{\epsilon}{k} - C_2 \frac{\epsilon^2}{k} + C_3 (T^*)^{C_4} \frac{Pr^2}{k} \right] \quad (8)$$

where C_1 , C_2 , C_3 , and C_4 are modeling constants, and T^* is a ratio of local to ambient temperature which when raised to the C_4 power⁴. This model reduces the apparent turbulent viscosity across temperature gradients. The results, as shown in Figures 5 and 6, demonstrate that with the temperature correction model the film cooling is predicted to be more effective. However, compared to the result of the ideal gas model, the liquid RP-1 coolant is less effective than the gas RP-1 coolant. This is because the momentum of the liquid RP-1 is smaller than that of gas RP-1. In order to model the liquid RP-1 coolant flow more accurately, a small-gap case was simulated where the RP-1 coolant is injected at the coolant hole location as described in Table 7. As with the previous case, the same two mixing models were employed, and the results are shown in Figures 7 and 8.

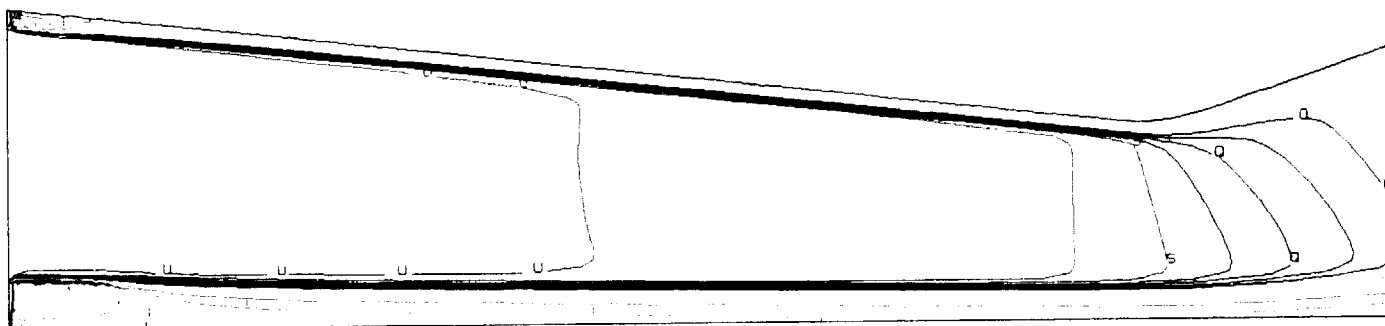
Figure 9 and Table 8 summarize these simulations. The lowest predicted wall temperatures are believed to be the most accurate. The C^* efficiency values are thought to be realistic. Additional work is required to evaluate the effect of the ablative liner response to this predicted wall temperature distribution.

3.2 GO₂/GH₂ Shear Coaxial Injector

Due to the lack of definitive test data on a tripropellant injector element, several injector configurations were simulated to evaluate the homogeneous spray combustion model in a piecemeal fashion. Santoro and his co-workers at PSU investigated several coaxial injector elements^{1,2,17}. These consisted of GO₂/GH₂, LO₂/GH₂, and RP-1/GH₂/GO₂ injectors. All of these injectors were numerically simulated to evaluate various aspects of the CFD modeling.

The GO₂/GH₂ shear coaxial injector test case¹, was simulated to validate the capability of the proposed model to predict mixing and chemical reaction phenomena. This test case is the first experiment which was designed to provide very detailed injector flow data. Measurements included: mean flow, root-mean-square fluctuation velocities, OH radiance, and stable species concentrations for high pressure combustion. A uni-element shear coaxial injector, as sketched in Figure 10, was used to introduce the propellants into the combustion chamber. The numerical simulations are for a computational domain which starts 25.4 mm upstream and stops 8 inches downstream from the injector face. The inlet conditions of the propellants are listed in Table 9. The H₂/O₂ combustion was assumed to occur under conditions of local chemical equilibrium which are appropriate at these pressures. The numerical results are compared to the test case as shown in Figures 11-12. The simulated flowfield is plotted in terms of temperature and is illustrated in Figure 13. The agreement between the numerical results and the test data are very good except for the H₂O mole fraction. In Fig. 11, the growth of shear layer is shown to be well predicted which indicates the turbulent mixing and the chemical reaction are simulated accurately. The major part of the discrepancy between the measurements and the predictions for the GO₂/GH₂ injector are attributed to inaccuracies in the measurements. For example, if the reported water measurements are correct, very little combustion would have occurred. This is not consistent with the good agreement obtained between the predicted and measured velocity

Temperature (deg K, liquid RP-1/hot gas mixture)



XMIN -5 0674E-01
XMAX 2 0776E+01
YMIN -6 5681E+00
YMAX 1 1168E+01

FMIN 2 9556E+02
FMAX 3 7343E+03
DELF 1 7009E+02

CONTOUR LEVELS

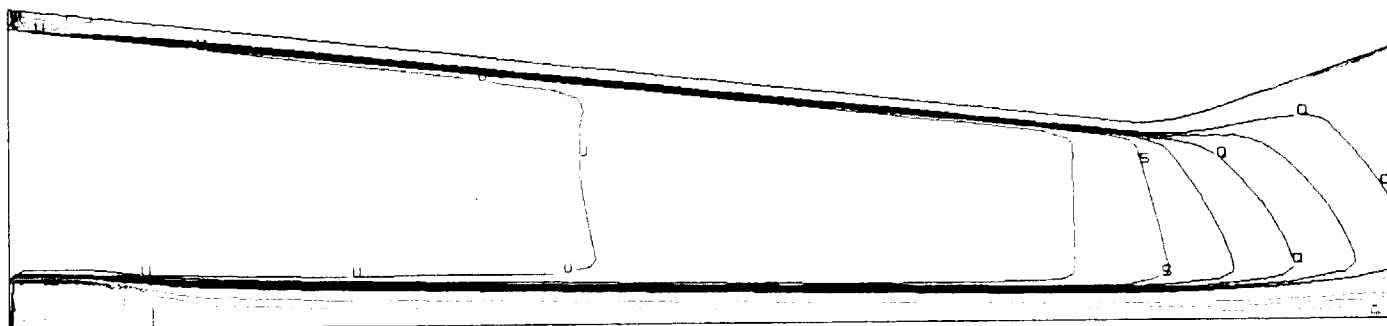
ID VALUES
A 2 9840E+02
B 4 6850E+02

C 1 8100E+02
D 1 4000E+02
E 1 0500E+02
F 1 0000E+02

G 2 6797E+03
H 2 8498E+03
I 3 0198E+03
J 3 1899E+03
K 3 3600E+03
L 3 5301E+03
M 3 7002E+03

Figure 5

Temperature (deg K, liquid RP-1/hot gas mixture, T-correctio



XMIN -5 0674E-01

XMAX 2 0776E+01

YMIN -5 5681E+00

YMAX 1 1168E+01

FMIN 2 9556E+02

FMAX 3 7344E+03

DELTA 1 7009E+02

CONTOUR LEVELS

ID VALUES

A 2 9840E+02

B 4 6850E+02

Q 2 6797E+03

P 2 8498E+03

R 3 0198E+03

S 3 3600E+03

T 3 5301E+03

U 3 7002E+03

Q 2 6797E+03

P 2 8498E+03

R 3 0198E+03

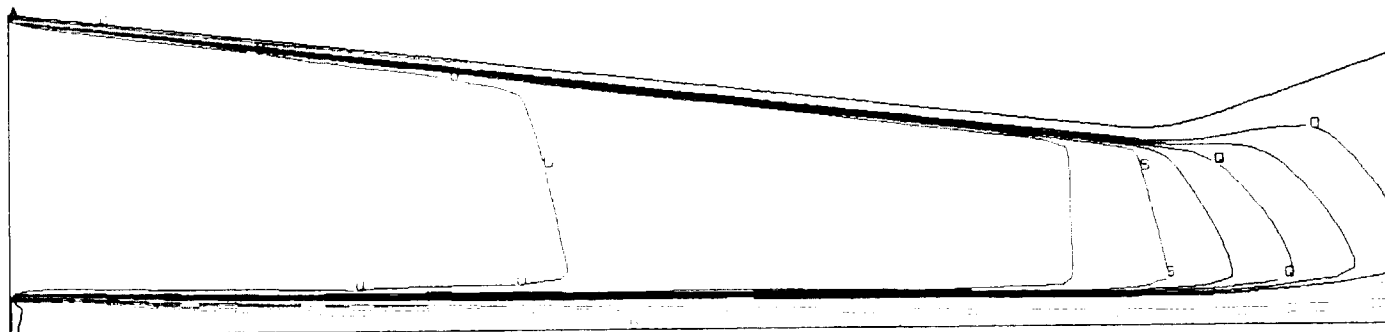
S 3 3600E+03

T 3 5301E+03

U 3 7002E+03

Figure 6

Temperature (deg K, liquid RP-1/hot gas mixture)



XMIN -5 0674E-01

XMAX 2 0776E+01

YMIN -6 5681E+00

YMAX 1 1168E+01

FMIN 2 9555E+02

FMAX 3 7321E+03

DELF 1 7009E+02

CONTOUR LEVELS

ID VALUES

A 2 9840E+02

B 4 6850E+02

C 6 3860E+02

D 8 0870E+02

E 1 0081E+03

F 1 9291E+03

G 2 8501E+03

H 3 7711E+03

I 4 6921E+03

J 5 6131E+03

K 6 5341E+03

L 7 4551E+03

M 8 3761E+03

N 9 2971E+03

O 1 0081E+04

P 1 9291E+04

Q 2 8501E+04

R 3 7711E+04

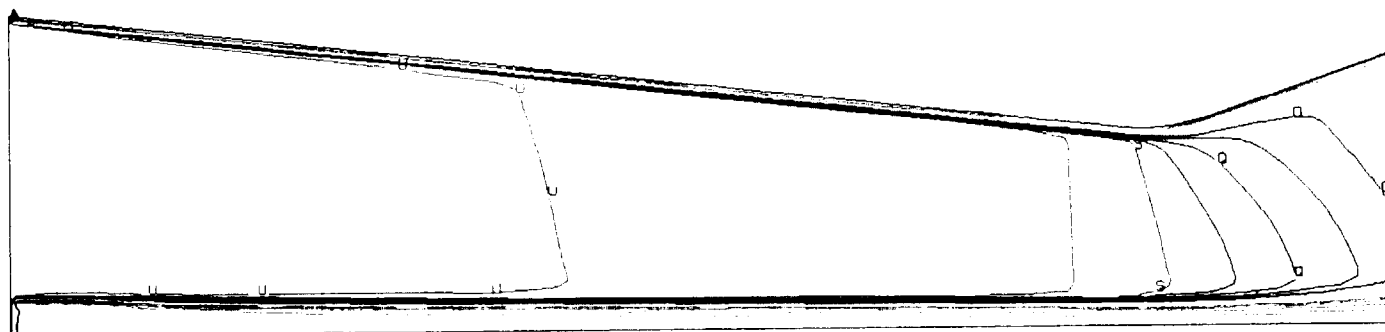
S 4 6921E+04

T 5 6131E+04

U 6 5341E+04

Figure 7

Temperature (deg K, liquid RP-1/hot gas mixture, T-correctio



XMIN -5 0674E-01

XMAX 2 0776E+01

YMIN -6 5681E+00

YMAX 1 1168E+01

FMIN 2 9555E+02

FMAX 3 7329E+03

DELF 1 7009E+02

CONTOUR LEVELS

ID VALUES

A 2 9840E+02

B 4 6850E+02

C 1 5194E+02

D 1 4000E+02

E 1 3400E+02

F 1 2800E+02

G 2 6797E+03

H 2 8498E+03

I 3 0198E+03

J 3 1899E+03

K 3 3600E+03

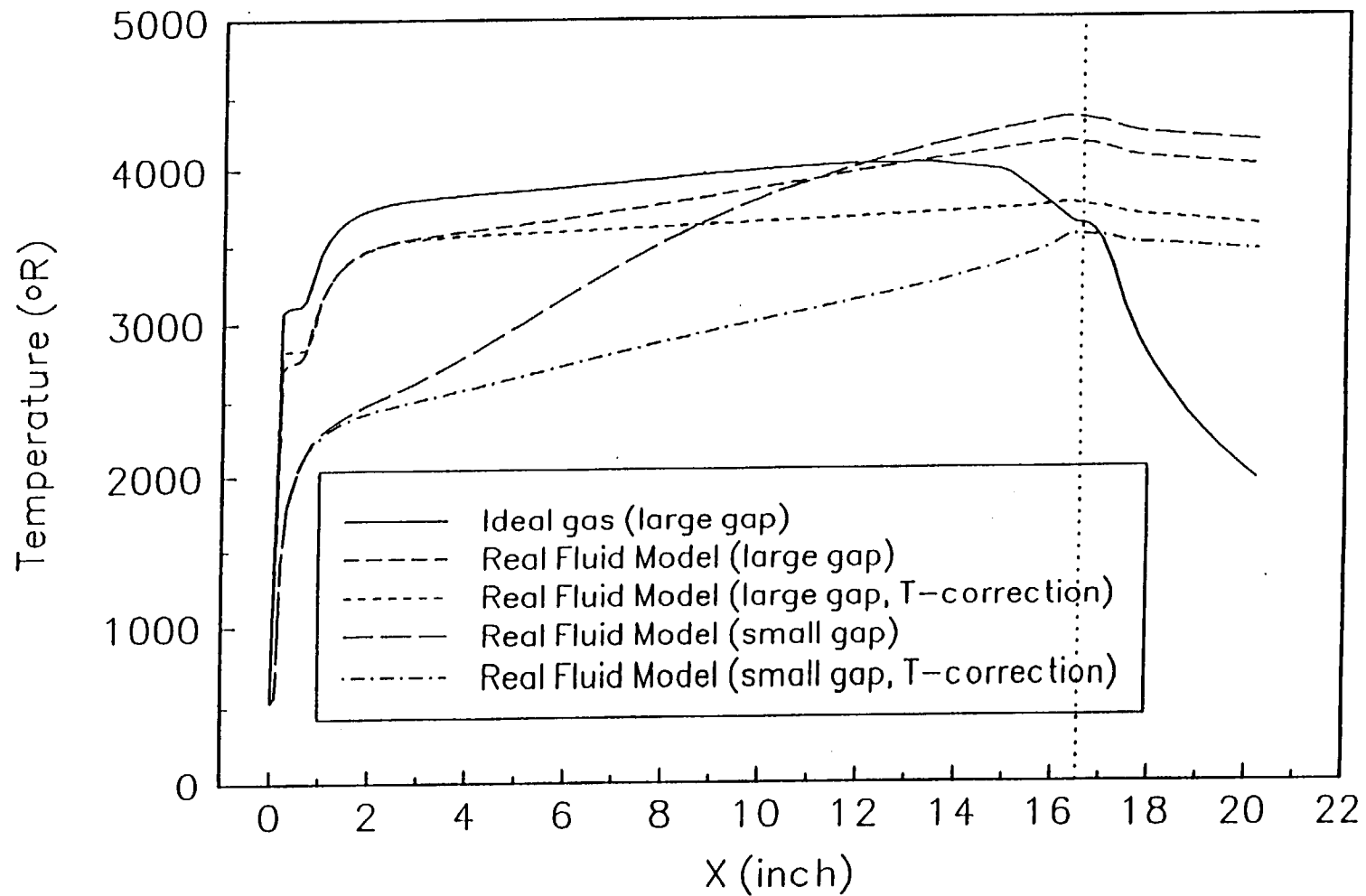
L 3 5301E+03

M 3 7002E+03

Figure 8

Figure 9

TEMPERATURE DISTRIBUTION ALONG NOZZLE WALL (Frozen Chemistry)



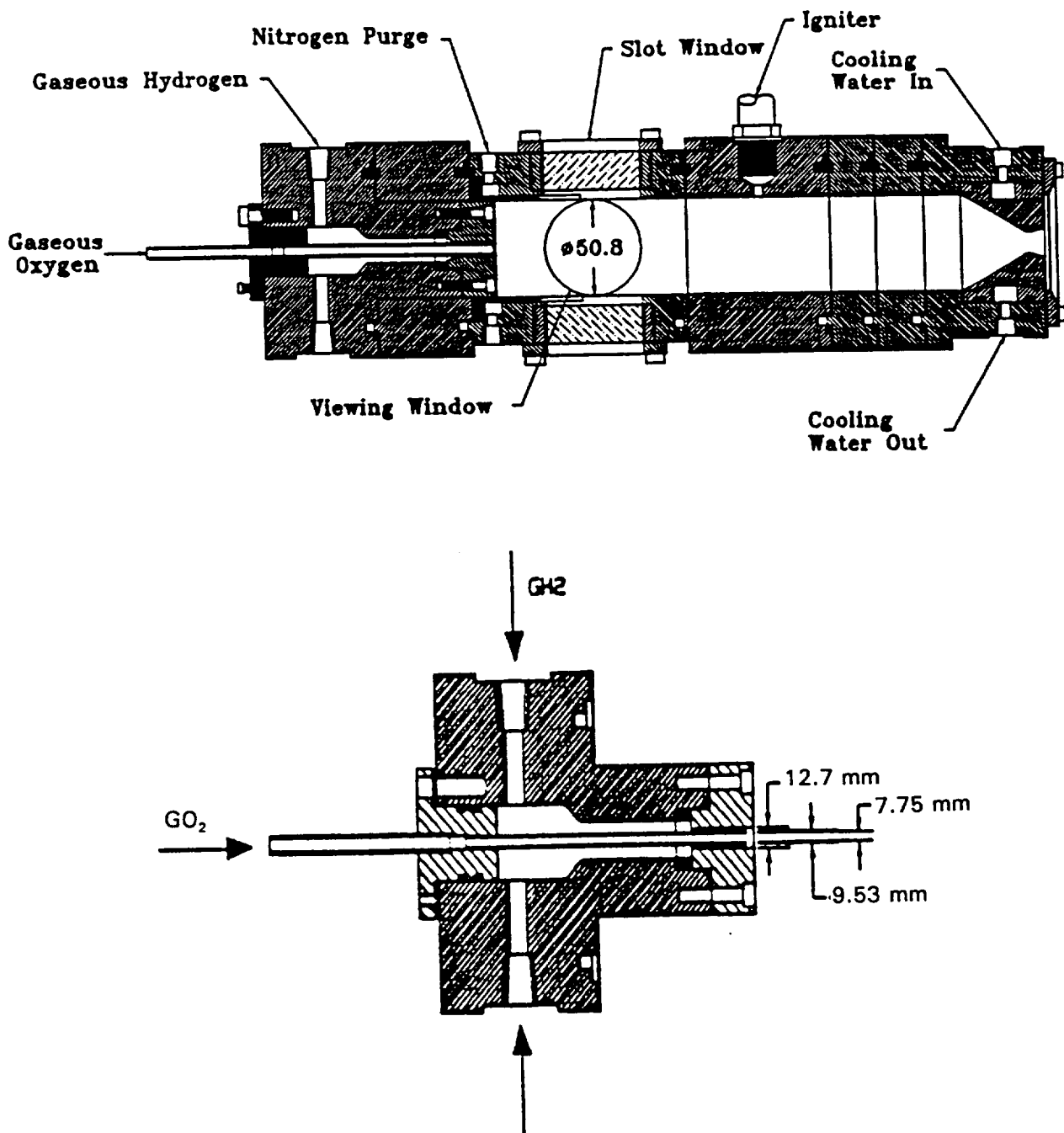


Figure 10. The Schematic of the Uni-element Shear Coaxial Injector Test Facility

Table 9. The Inlet Flow Conditions of the GO_2/GH_2 Injector Test Case

	GO_2	GH_2
Pressure (MPa)	1.31	1.31
Temperature ($^{\circ}\text{K}$)	290	298
Mass flow rate (kg/s)	0.04196	0.0104
Axial velocity (m/s)	51.1	177.2

Table 10. The Inlet Flow Conditions of the LO_2/GH_2 Injector Test Case #1

	LO_2	GH_2
Pressure (psi)	453	453
Temperature ($^{\circ}\text{R}$)	210	557
Density (lb/ft^3)	62.79	0.1516
Mass flow rate (lb/s)	0.397	0.049

Table 11. The Inlet Flow Conditions of the LO_2/GH_2 Injector Test Case #2

	LO_2	GH_2
Pressure (psi)	260	260
Temperature ($^{\circ}\text{R}$)	210	557
Density (lb/ft^3)	62.42	0.0864
Mass flow rate (lb/s)	0.371	0.073

profiles. Furthermore, the summation of the measured mole fractions is not close to unity. This difference cannot be solely attributed to unmeasured radicals. Temperature measurements were not reported, but verbal reports indicated that temperature was estimated to be about 3000 $^{\circ}\text{K}$ in the shear layer. The discrepancy between the measurements and the numerical predictions for the velocity near the chamber wall is caused by the nitrogen purge used to protect the optical windows. The purge flow was not accounted for in the numerical simulations. As far as the fluctuating velocity is concerned, the disagreement in the comparison is anticipated because the values of the axial fluctuating velocity are calculated from the turbulence kinetic energy, assuming isotropy. This assumption is widely recognized to be inaccurate for turbulent jet flows, hence its use probably accounts for the predicted isotropic axial fluctuating velocities being smaller than the measured values. None of the comparisons made in this evaluation suggest that any modifications to the CFD model are necessary.

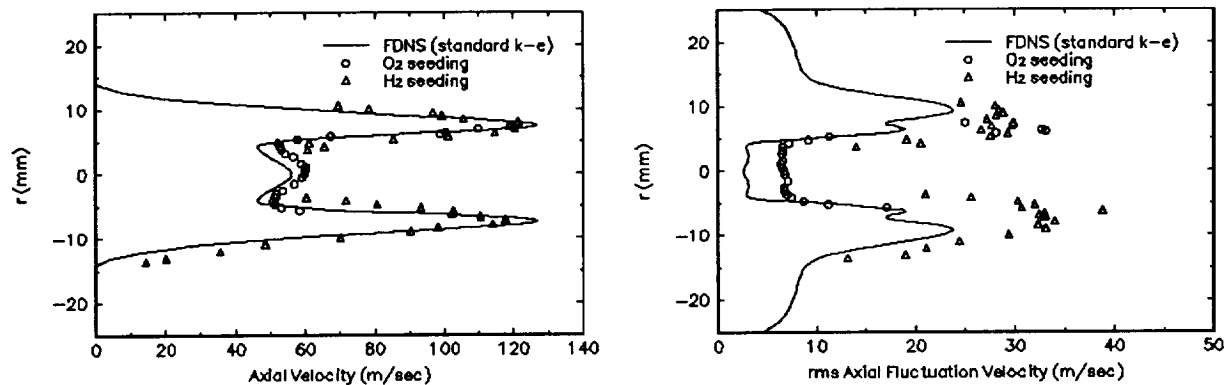
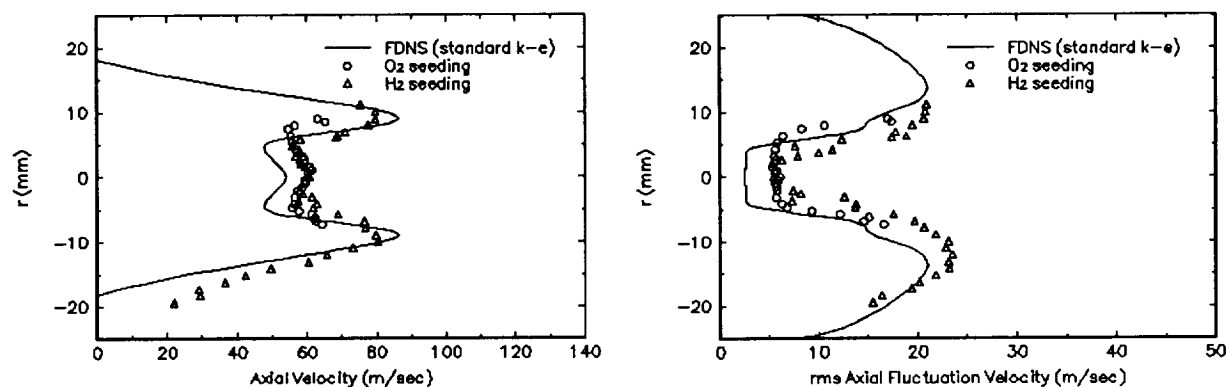
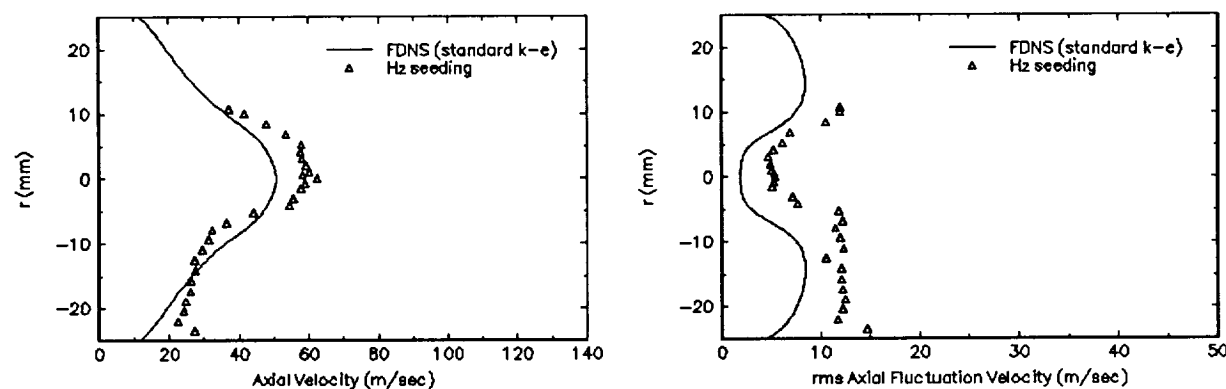
(a) $x = 25.4$ mm(b) $x = 50.8$ mm(c) $x = 127$ mm

Figure 11 Comparison Between Measured and Calculated Mean and Root-Mean-Square Axial Velocities for Three Axial Locations (equilibrium chemistry)

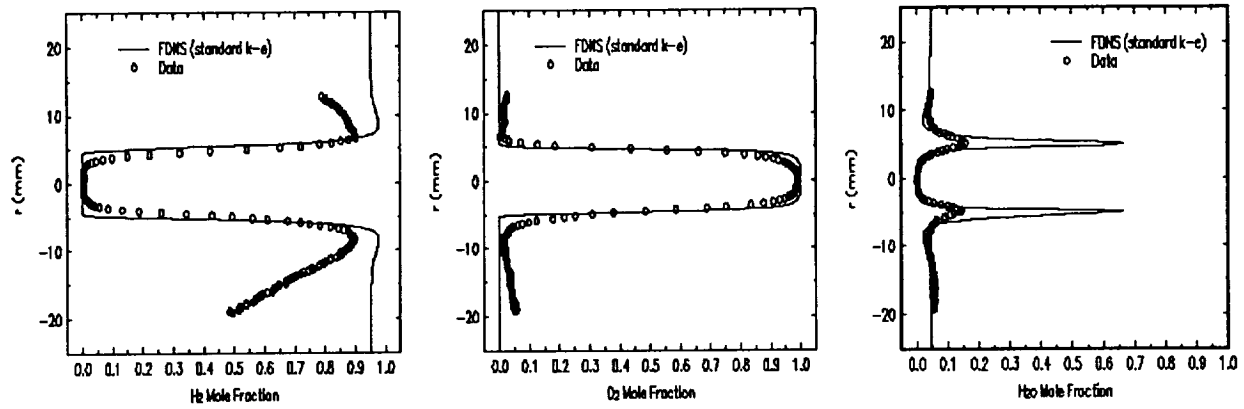
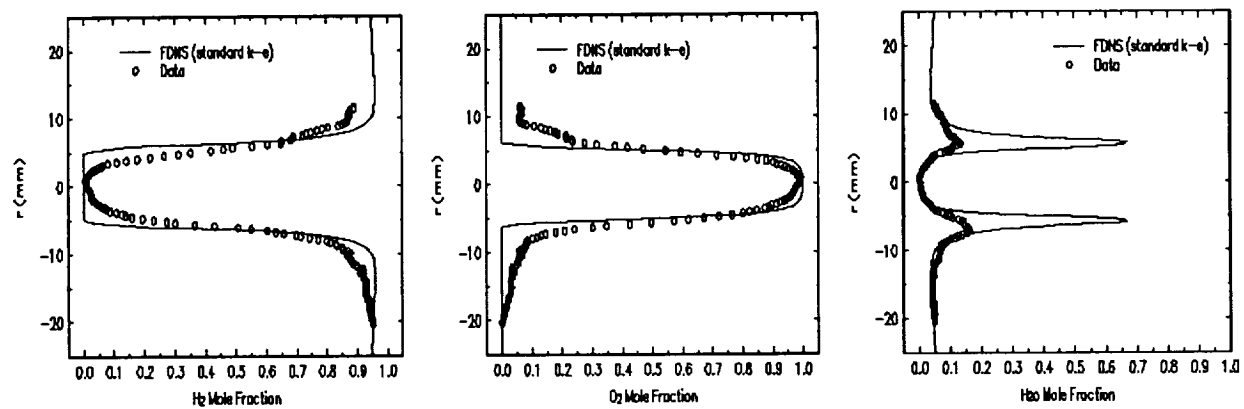
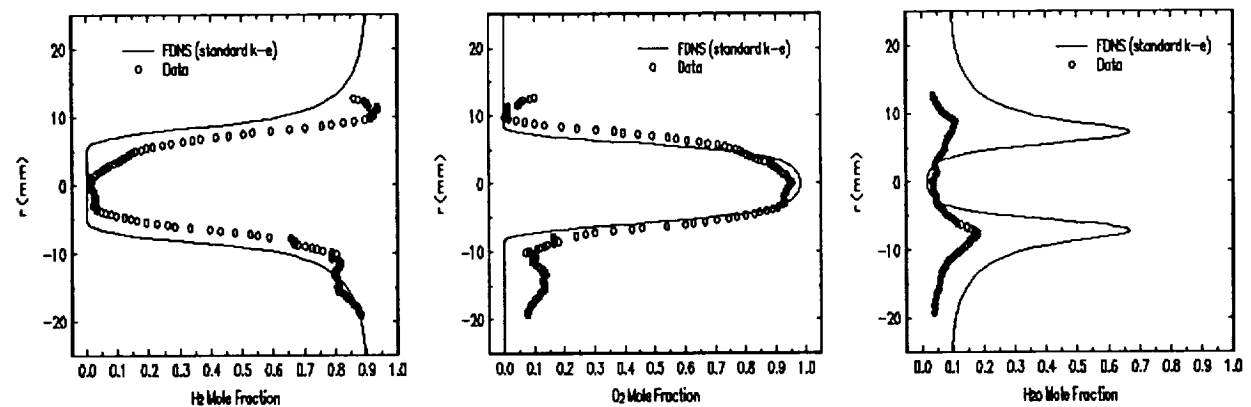
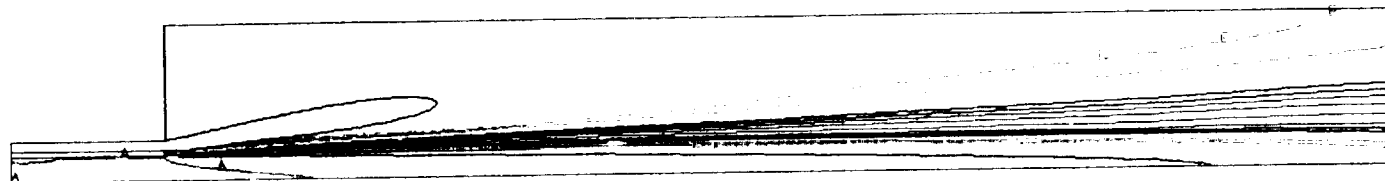
(a) $x = 25.4$ mm(b) $x = 50.8$ mm(c) $x = 127$ mm

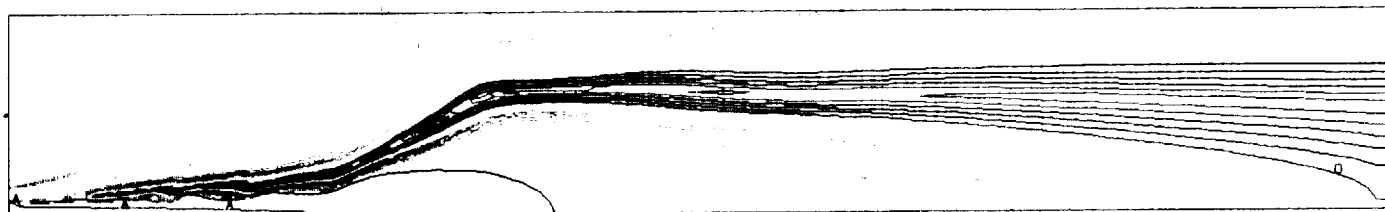
Figure 12 Comparison Between Measured and Calculated Species Concentrations for Three Axial Locations (equilibrium chemistry)

Figure 13 Predicted Temperature Contours for the GO_2/GH_2 Inject Flow

ID	VALUES
A	2 9000E+02
B	5 8000E+02

C	1 4000E+02
D	1 7000E+02

I	2 6099E+03
J	2 9000E+03
K	3 1900E+03
L	3 4800E+03

Figure 14 Predicted Temperature Contours for the LOX/GH_2 Injector Test Case #1

ID	VALUES
A	1 1758E+02
B	2 8190E+02

C	1 1000E+02
D	1 1000E+02
E	1 1000E+02
F	1 1000E+02

Figure 15 Predicted Temperature Contours for the LOX/GH_2 Injector Test Case #2

O	2 4179E+03
P	2 5823E+03
Q	2 7466E+03
R	2 9109E+03
S	3 0752E+03
T	3 2395E+03
U	3 4038E+03

3.3 LO₂/GH₂ Shear Coaxial Injector

Two LO₂/GH₂ shear coaxial injector flow test cases, also examined by Santoro and his coworkers², were predicted to further validate the real fluid homogeneous spray combustion model. The expectation was that the homogeneous spray combustion model would underpredict the mixing, since droplet generation and dispersion was not simulated. The configuration of the experiment was similar to that of the gas/gas injector test case, except that liquid oxygen flowed through the inner tube. The inner tube diameter was 3.42 mm, and the gas hydrogen flowed through the outer annulus. The inner and outer diameters of the annulus were 4.19 mm and 7.11 mm, respectively. The nozzle was changed to provide the desired test pressure. The inlet conditions of the propellants for both test cases are listed in Tables 10-11. A global kinetics chemistry for H₂/O₂, listed in Table 4, was employed to model the spray combustion because the cold temperatures suggested that finite-rate effects could be important. The calculated results for both cases are plotted as shown in Figures 14-15.

Test data for sub-critical combustion were reported to indicate a growing jet of LO₂ spray even at the downstream end of the computation domain. Predicted temperatures are about 3000°K, suggesting the presence of drops is unlikely. No mechanism has yet been suggested by these investigators or others for explaining LO₂ drops at these high gas temperatures. If the mixing and/or combustion is reduced in the model to allow for the presence of LO₂, the predicted combustion efficiency would be quite low. For combustion experiments, the primary measurement of interest is temperature. However, temperature has not been reported, therefore, no modification to the CFD model was made.

3.4 Tripropellant Shear Coaxial Injector Elements

The third test case simulated with the homogeneous spray combustion model was a tripropellant (GO₂/GH₂/RP-1) shear coaxial injector flow, also examined by Santoro and his coworkers¹⁷. The schematic of the injector element is sketched in Figure 16. The hydrogen gas is assumed to be fully mixed with RP-1 and injected into the combustion chamber through the inner tube of 0.15 in. diameter. The mass flow rates of GH₂ and RP-1 are 0.015 lb/sec and 0.15 lb/sec, respectively. The gaseous oxygen has a mass flow rate of 0.48 lb/sec and is injected through the annulus, which has inner and outer diameters of 0.18 in. and 0.5 in., respectively. The combustion chamber is modeled for 7 in. downstream from the injector face. The chamber pressure is 500 psi and the temperature of all propellants is 540 °R. The combustion is represented with three global kinetics expressions, as shown in Table 3, to simulate RP-1 oxidation, soot formation, and soot oxidation process, where the RP-1 oxidation step produces H₂ and CO. The combustion was completed with a wet CO equilibrium model. Hence, ignition delays may arise only from the RP-1 oxidation step.

The predicted temperature field and regions of soot formation are shown in Figs. 17 and 18, respectively. The flow is predicted to be highly striated, but all of the RP-1 is vaporized in the first 3 in. of the combustor. Drops with a mean size of 20 μm were reported at a point 6 in. from the injector face and 0.2 in. off of the centerline, even though the combustion efficiency is reported to be 97.5%. Drop size distributions and velocities were reported for this point; however, the total flowrate of RP-1 liquid cannot be estimated from these data. The

velocity predictions and measurements are in close agreement, even though insufficient test data are available to identify weak points in the analysis. The soot mass fraction predictions are very low. However, soot is predicted where it would be expected. The soot model can be easily tuned, if suitable test data were available.

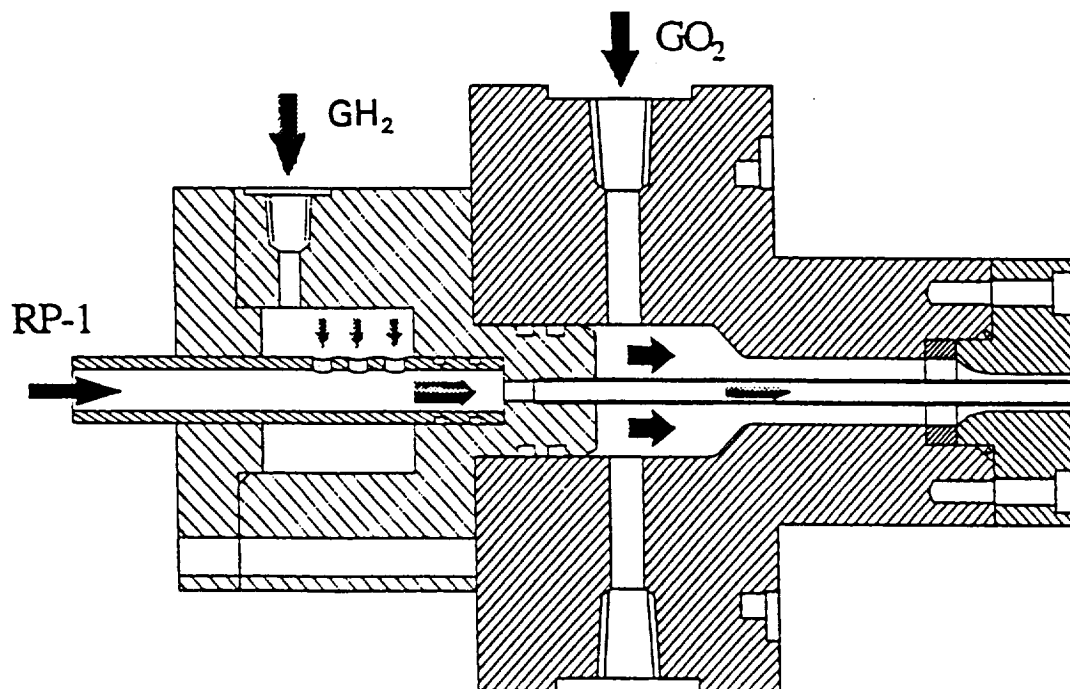
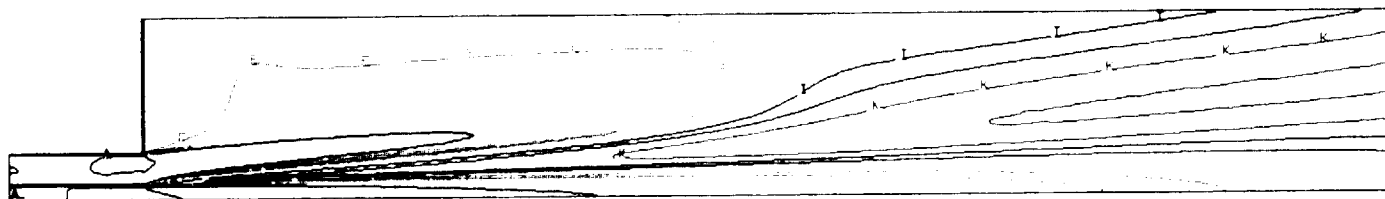


Figure 16. Schematic of Injector Element Used for RP-1/GH₂/GO₂ tripropellants

Temperature (deg K, GOX/GH2/RP-1 shear coaxial)



XMIN -9 4374E-01

XMAX 7 1937E+00

YMIN -2 8906E+00

YMAX 3 8906E+00

FMIN 2 9907E+02

FMAX 3 6657E+03

DELF 3 0000E+02

CONTOUR LEVELS

ID VALUES

A 3 0000E+02

B 6 0000E+02

I 2 7000E+03

J 3 0000E+03

K 3 2999E+03

L 3 5999E+03

I 2 7000E+03

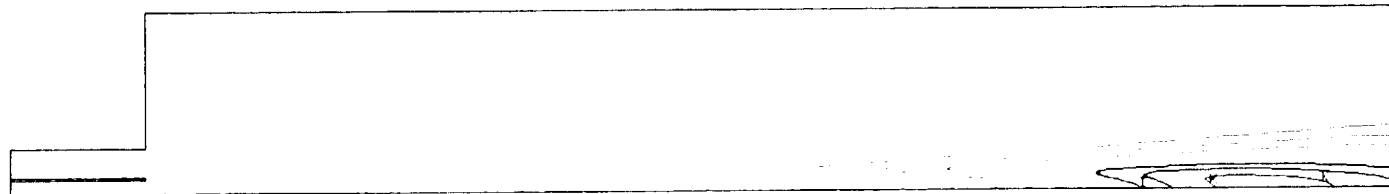
J 3 0000E+03

K 3 2999E+03

L 3 5999E+03

Figure 17

Mass fractions of soot (GOX/GH2/RP-1 shear coaxial injector)



XMIN -9 4374E-01
XMAX 7 1937E+00
YMIN -2 8906E+00
YMAX 3 8906E+00

FMIN 0 0000E+00
FMAX 3 6427E-06
DELF 3 5000E-07

CONTOUR LEVELS

ID	VALUES
A	0.0000E+00

1	1.0000E-06
2	2.0000E-06
3	3.0000E-06

H	2 4500E-06
I	2 7999E-06
J	3 1500E-06
K	3 5000E-06

Figure 18

3.5 Fastrack Injector Elements

After the firing of early versions of the Fastrack motor, the liner near the injector face plate showed locally excessive ablation. The large ablation occurred in streaks in the axial direction with the number of streaks, as well as the distribution of streaks over the wall in the circumferential direction, being dependent on the design of the injector face plate¹⁸.

The objective of the CFD analysis of the near-injector-flow was to determine a possible source of the observed ablation phenomenon. For this investigation, the flow within a region of the motor that was bounded by a section of the injector face plate and the wall of the combustion chamber was modeled in detail. The section of the injector face plate used in the CFD modeling involved a pair (doublet) of oxidizer holes, a pair (doublet) of fuel holes, and three holes for film-cooling flow. Recognizing the symmetric nature of the flow under consideration with respect to the azimuthal direction allowed the flow to be computed for only one half of the injector face plate element with symmetry boundary conditions imposed to account for the other half. The face plate section modeled in the CFD analysis can be identified by referring to Fig. 2.

The orientation based on a coordinate system erected in the center of the injector face and some dimensions of the volume treated by the CFD analysis are shown in Figure 19.

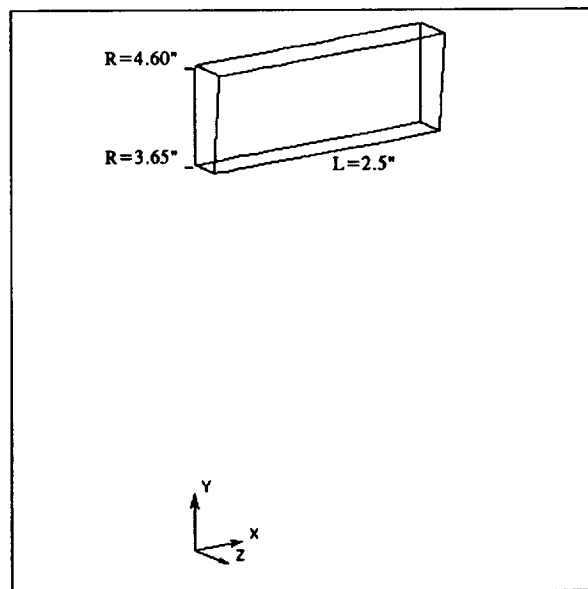


Figure 19: Volume Element Used for CFD Analysis.

The details of the face plate section bounding the volume plotted in Figure 19 are shown in Figure 20. As shown in Figure 20, the computational domain consists of one LO₂ injector hole, one RP-1 injector hole, and one and one half RP-1 coolant injector holes.

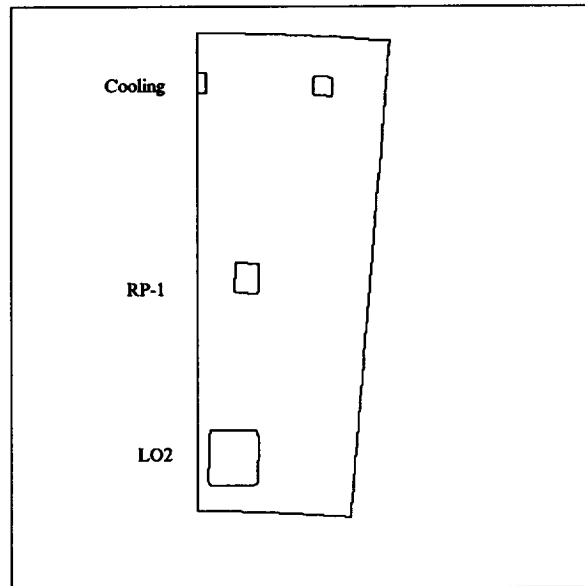


Figure 20: Injector Holes in Modeled Face Plate Section.

Although the cross-sections of the injector holes in the CFD modeling are essentially rectangular, the area of each hole is the same as the corresponding cross-sectional area of the (elliptical) hole in the physical case.

The computational grid consisted of 31 planes in the axial direction, with each plane employing 41 nodes in the radial direction, and 21 nodes in the azimuthal direction. A non-uniform grid spacing was selected in the axial direction with the grid points being packed more closely towards the injector face, thus allowing for a better resolution of the flow in the immediate vicinity of the injector. The grid points in both, the radial and the azimuthal are clustered in the injector hole regions to accurately capture the incoming mass-flows. The three-dimensional computational grid is shown in Figure 21.

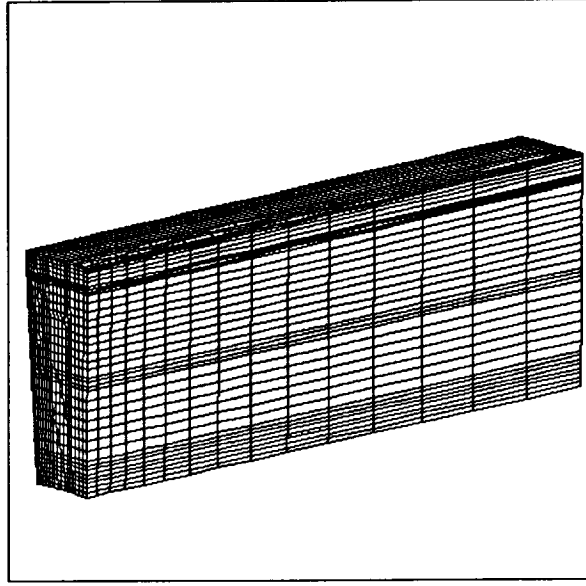


Figure 21: Computational Grid Involving 31x41x21 Nodes.

A summary of the initial conditions for the different mass-flows entering the control volume is given in Table 12. The axial component of the velocity is implied by the mass flowrate. The other two components of the total velocity vector were calculated based on the orientation of each hole. The angles used for the calculations were taken from drawings supplied by NASA. The resulting total velocity vectors for the injected mass-flows are plotted in Figure 22.

Table 12. The Inlet Flow Conditions for the Fastrack Injector Face Simulation

	LO ₂ Hole	RP-1 Hole	RP-1 Coolant
Area per hole (in ²)	0.007726	0.002432	0.001077
Mass flow rate per hole (lb/s)	0.4042	0.1482	0.0291
Temperature (°R)	190	532	532
Density (lb/ft ³)	67	46.5	46.5
Pressure (psi)	514	514	514

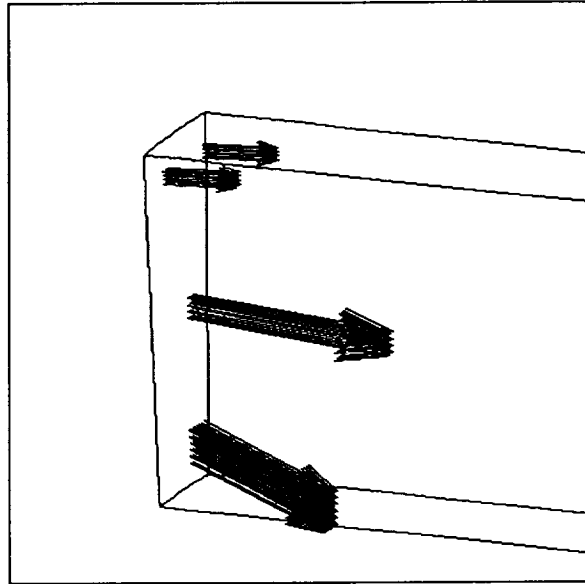


Figure 22: Total Velocity Vectors of Injected Mass-Flows.

Two numerical simulations of the flowfield near Fastrack injector face were conducted to analyze the effect of injector cant angles on the chamber wall heating. The first case corresponds to that just described. In Table 13, the impingement and cant angles of the LO_2 and RP-1 streams for two simulated cases are shown. For both cases, a symmetry condition was employed for the two boundaries in the circumferential direction. The top boundary in the radial direction is a wall; while the bottom boundary in the radial direction was assumed to be symmetry plane. The chemistry model used for the tripropellant injector was also used for this case. The flow angle of case #1 is the original design. The numerical results of case #1, as shown in Figure 23, indicates that a strong cross-stream secondary flow structure and a streamwise flow recirculation was induced due to the radial velocity component resulting from the propellant cant angles as well as the slip boundary condition imposed on the bottom surface. The oxygen and RP-1 flows were well mixed downstream of the impingement surface, and then was carried as secondary flow back towards the impingement surface and toward the top wall. Also, the propellant mixture recirculated towards, and heated, the injector face, and followed the same secondary flow structure. As a result, the hot streak on the wall occurred between the RP-1 coolant holes and aligned with the propellant injector holes. Though the strength of the secondary flow could have been over-predicted due to the slip boundary condition assumption of the bottom surface, the induction of the secondary flow is reasonable because of the large opening between the impingement point and the top wall.

To reduce the severity of the induced secondary flow, a second test case was simulated, for which the cant angle for both the oxidizer and fuel flow was eliminated. The elimination of the flow cant angle makes the assumed slip boundary condition of the bottom surface less critical. As anticipated, the numerical results, as shown in Figure 24 reveal that a much weaker

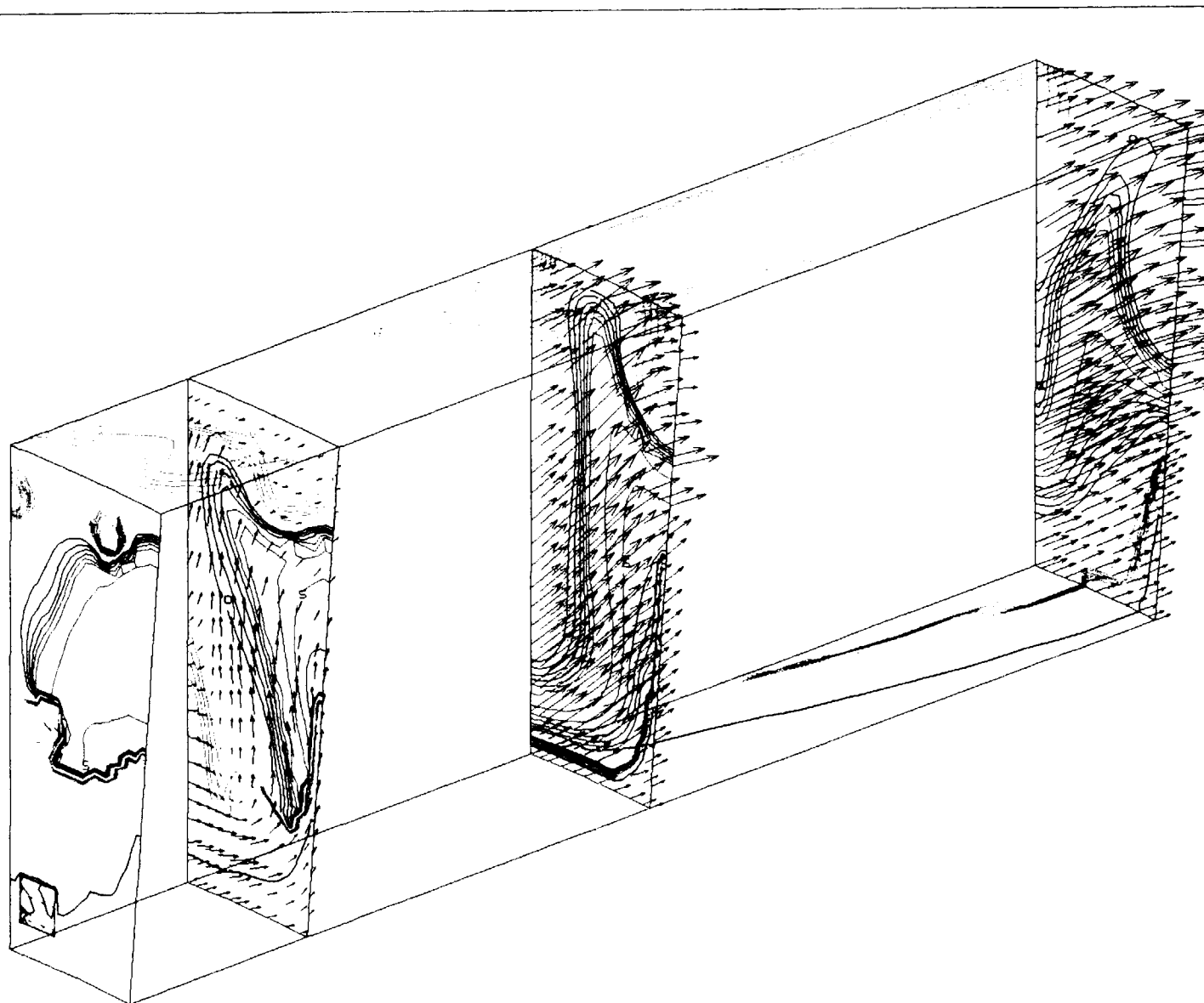
Table 13. The Impingement and Cant Angles of the Propellants for Both Cases

	Case #1	Case #2
LO ₂ impingement angle	30°	30°
LO ₂ cant angle	50°	0°
RP-1 impingement angle	25°	25°
RP-1 cant angle	27°	0°

secondary flow, compared to that in case #1 was induced. As a result, the wall temperature is much lower and more uniform. Meanwhile, the region of stoichiometric mixture is much thinner compared to that in case #1 and is formed between the LO₂ doublet and the RP-1 doublet. This indicates that secondary flows enhance mixing, but a compromise must be made to reduce wall heating vs. optimizing performance.

Further study to add the inner rows of injector holes and thus reduce the sensitivity to the assumption of the slip boundary condition is recommended. Also, a gas only solution for the boundaries of the detailed injector element should be considered. Other alternatives to this homogeneous spray analysis could be devised, however, this methodology is believed to yield the most realistic flowfield information for the computation required for the analysis. The computation time required for these analyses was long, but further optimization and some additional simplification could be realized.

Fast-Track near Injector Simulation (no Cavity)



XMIN -3 0484E-02
 XMAX 2 1416E+00
 YMIN 3 1860E+00
 YMAX 4 9961E+00

FMIN 1 0554E+02
 FMAX 3 7523E+03
 DELF 1 8472E+02

CONTOUR LEVELS

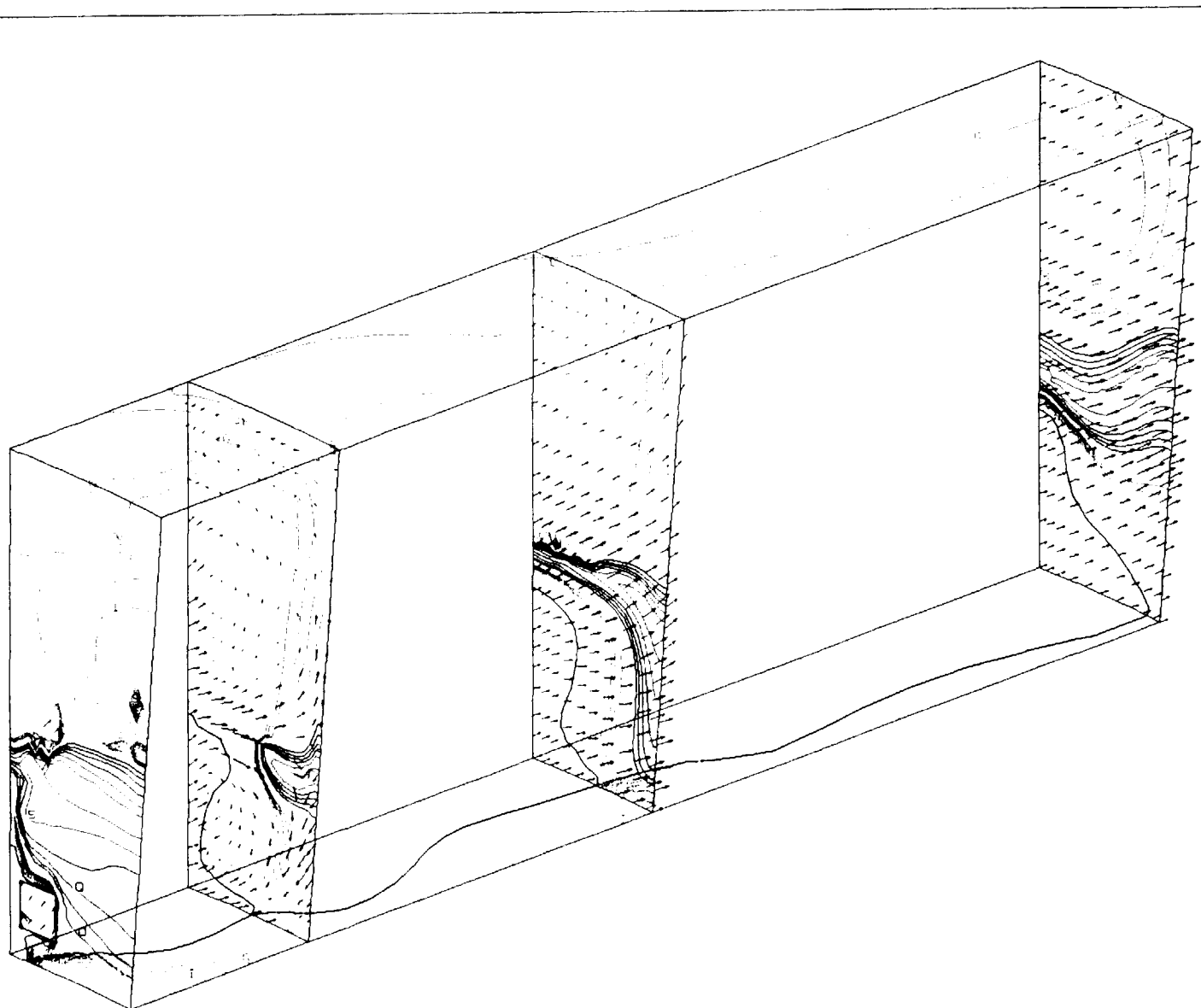
ID	VALUES
A	1 0555E+02
B	2 9027E+02

ID	VALUES
V	1 1111E+00
W	1 1111E+00
X	1 1111E+00
Y	1 1111E+00

D	2 6916E+03
P	2 8763E+03
Q	3 0611E+03
R	3 2458E+03
S	3 4305E+03
T	3 6152E+03
U	3 7999E+03

Figure 23

Fast-Track near Injector Simulation (no Cavity)



```
XMIN  -3  0484E-02
```

```
XMAX      2  1416E+00
```

```
YMIN      3  1860E+00
```

```
YMAX      4  9961E+00
```

```
FMIN      1 0515E+02
```

```

FMAX      3  7253E+03

```

DELFT 1 8472E+02

CONTOUR LEVELS

ID	VALUES
----	--------

A. 1.0555E+02

B 2.9027E+02

• 4 •

$$p_1 = 1 - \frac{1}{2} - \frac{1}{2} = 0, \quad p_2 = \frac{1}{2} + \frac{1}{2} = 1.$$
$$1 \quad 1 \quad 2 \quad 3 \quad 4 \quad 5$$

1. *U. glaberrima* (L.)

0 2 6916E+03

P 2 8763E+03

Q 3 0611E+03

```
R      3  2458E+03
```

5 3 4305E+03

T 3 6152E+03

U 3 7999E+03

Figure 24

4.0 CONCLUSIONS & RECOMMENDATIONS

Conclusions drawn from this investigation are:

- (1) The FDNS-RFV code is a useful analysis tool for evaluating near injector-face flowfields of tripropellant and bipropellant liquid motor injector element designs.
- (2) Experiments performed to characterize injector element configurations should be conducted in closer concert with analytical studies to insure that they produce sufficient test data to serve as verification of the applicable flowfield analysis. In particular, local temperature measurements are essential to validate a combustion model.

Recommendations for future use of this CFD design code are:

- (1) Additional cases be analyzed with the FDNS-RFV code to determine the best method of synthesizing this detailed analysis with appropriate analyses of bounding flows. The use of multiple rows of injector elements and of gas only (or gas/spray) coarse grid analyses to serve as boundary conditions for detailed injector element analyses should be investigated.
- (2) The extension of this homogeneous spray combustion model to account for, even in an approximate fashion, the presence of spray drops should be considered. For example, finite-rate vaporization within the homogeneous spray combustion code is a simple extension which could prove quite useful.

5.0 REFERENCES

1. Beisler, M.A., Pal, S., Moser, M.D., and Santoro, R.J., "Shear Coaxial Injector Atomization in a LO_2/GH_2 Propellant Rocket," AIAA Paper 94-2775, 1994.
2. Moser, M.D., Pal, S., and Santoro, R.J., "Laser Light Scattering Measurements in a GO_2/GH_2 Uni-Element Rocket chamber," AIAA 95-0137, 1995.
3. Cheng, G.C., Chen, Y.S., and Wang, T.S., "Flow Distribution Within the SSME Main Injector Assembly Using Porosity Formulation," AIAA 95-0350, 1995.
4. Cheng, G.C., Farmer, R.C., and Chen, Y.S., "Numerical Study of Turbulent Flows with Compressibility Effects and Chemical Reactions," AIAA Paper 94-2026, 1994.
5. Chen, Y.S., Cheng, G.C., and Farmer, R.C., "Reacting and Non-Reacting Flow Simulation for Film Cooling in 2-D Supersonic Flows," AIAA Paper 92-3602, 1992.
6. Saad, Y., and Schultz, M.H., SIAM J. Sci. Stat. Comput., 7, pp. 856-869, 1986.
7. Chen, Y.S., and Kim, S.W., "Computation of Turbulent Flows Using an Extended k- ϵ Turbulence Closure Model," NASA CR-179204, 1987.
8. Liakopoulos, A., "Explicit Representations of the Complete Velocity Profile in a Turbulent Boundary Layer," AIAA Journal, Vol. 22, No. 6, June 1984, pp. 844-846.
9. Viegas, J. R., Rubesin, M. W., and Horstman, C. C., "On the use of Wall Functions as Boundary Conditions for Two-Dimensional Separated Compressible Flows," AIAA Paper 85-0180, AIAA 23rd Aerospace Sciences Meeting, Jan. 14-17, 1985.
10. Farmer, R.C., P.G. Anderson, and G.C. Cheng, Progress Reports on "Propulsion Chemistry for CFD Applications, under NAS8-40574, SECA, Inc., Huntsville, AL, ongoing.
11. Hirschfelder, J.O., et. al., Ind. & Engr. Chem., 50, pp. 375-385, 1958.
12. Hirschfelder, J.O., et. al., Ind. & Engr. Chem., 50, pp. 386-390, 1958.
13. Farmer, R.C., and P.G. Anderson, "Propulsion Chemistry for CFD Applications, SECA, Inc., Huntsville, AL, July 1995.
14. Reid, R.C., et al, The Properties of Gases & Liquids, 4th Ed., McGraw Hill, NY, 1987.
15. Model, M., and R.C. Reid, Thermodynamics and It's Applications, 2nd Ed., Prentice Hall, 1983.
16. Peng, D.Y., and D.B. Robinson, "A Rigorous Method for Predicting the Critical Properties of Multicomponent Systems from an Equation of State," AIChE Journal, 23, No. 2, 1977.
17. Mouis, A.G.F., Pal, S., and Santoro, R.J., "Tripropellant Rocket Combustion Using A Mixed RP-1/ GH_2 Injector," 8th Annual Symposium on Space Propulsion, Penn State University, pp. 55-58, Oct. 30-31, 1996.
18. Sparks, D.L., NASA/MSFC, personal communication.

APPENDIX A

RADIATION EFFECTS

● Radiative Properties along a Line-of-Sight

Since scattering is negligible, the equation of transfer for a line of sight, s , through an absorbing and emitting medium, which is in local thermodynamic equilibrium, is used to identify and define the radiative properties.

$$(dI_\nu/ds) + k_\nu I_\nu = k_\nu I_{b,\nu} \quad (1)$$

where I_ν is the spectral intensity, $I_{b,\nu}$ is the Planck blackbody intensity, k_ν is the spectral absorption coefficient and ν denotes wave number. Integration of equation (1) over all wave numbers and along the line of sight from the point $s = L$ to the observer at $s = 0$ yields

$$I^-\{0\} = \int_0^\nu \int_0^L I_{b,\nu}\{s\} \exp \left[- \int_0^s k_\nu ds' \right] k_\nu\{s\} ds d\nu \quad (2)$$

$I^-\{0\}$ is the spectral intensity directed toward point 0 along line s .

The development of this equation closely follows that presented by Buckius & Tien [1]. A medium containing more than one component is characterized by the spectral absorption coefficient that is the sum of the spectral absorption coefficients of each species. With the transmissivity defined as

$$\tau_{\nu i}\{s\} = \exp \left[- \int_0^s k_{\nu i} ds' \right] \quad (3)$$

the transmissivity for a mixture of i components is

$$\tau_\nu\{s\} = \prod_i \tau_{\nu i}\{s\} \quad (4)$$

which is strictly valid only for monochromatic radiation although it is found to be true experimentally over finite spectral intervals [2]. The intensity in equation (2) becomes

$$I^-\{0\} = \int_0^\nu \int_0^L I_{b,\nu}\{s\} \left[- \frac{d\tau_\nu\{s\}}{ds} \right] ds d\nu \quad (5)$$

- Homogeneous Gray Model

The absorption and emission of radiant energy by a mixture of gases and particles is a function of the concentration, temperature, and pathlength. The radiative transfer calculation for a line of sight is, therefore, dependent upon the variation of these parameters along the pathlength. This can result in very complicated computations for mixtures of many components. For simplification, the temperature and pressure are often taken as constants resulting in a homogeneous path approximation. Another major simplification in the analysis is achieved if it is assumed that one mean value of the absorption coefficient can account for all spectral variations. These two approximations yield the homogeneous gray model.

For the absorption coefficient which is not a function of wave number or pathlength, equation (5) becomes

$$I^- \{0\} = (\sigma T^4 / \pi) [1 - \exp \{-KL\}] \quad (6)$$

where K is a total averaged absorption coefficient. The use of this homogeneous gray equation is dependent upon the definition of K. Experimental measurements are one method of determining the mean coefficient. For both soot and combustion gases K is a strong function of ν , therefore this simplification is not acceptable.

- Homogeneous Nongray Model

The intensity for a homogeneous path is obtained from equation (5) as

$$I^- \{0\} = \int_0^x I_{b\nu} [1 - \tau_\nu \{L\}] d\nu \quad (7)$$

The spectral variation of the transmissivity for an infrared radiating gas is due to the vibrational-rotational bands. The spectral dependence can be evaluated for practical calculations by either narrow or wide band methods [3]. In particular, the exponential wide band model [4] has been successfully employed for various combustion gases. The narrow band models are much more computationally intensive [5], but more importantly parameters for these models have been established from data on atmospheric and subatmospheric pressure flames. The wide band models are based on higher pressure flame data.

For a gaseous medium with a single vibrational-rotational band, the frequency dependence for a band is restricted to a small interval as compared to the blackbody spectrum. For this reason, $I_{b\nu}$ is removed from the integral in equation (7) and taken constant at the wavelength of the band head or center depending upon the type of band to give

$$I^- \{0\} = \overline{I_{b\nu}} A_{ij} \quad (8)$$

The use of equation (8) implies that the gas absorbs like a blackbody over the band frequency interval. This procedure yields the correct band absorbance, but cannot be conveniently averaged with the continuum soot absorbance in this frequency interval. Edwards [6] remedies this problem by defining a band transmissivity, τ_g , with the equation

$$\tau_g = d \ln A^* / d \ln \tau_H < 0.9 \quad (9)$$

where τ_H is the maximum optical depth at the band head. Hence,

$$A_{ij} = (1 - \tau_{g,j})(\nu_{u,j} - \nu_{l,j})A_{ij}^* = \omega A_{ij}^*$$

Further explanation of this process is shown in an example problem given by Edwards [4].

Use of wide band formulas for the integrated band intensity α_{ij} , the band width parameter ω_{ij} , the mean line width-to-spacing ratio β_{ij} , and the equivalent broadening pressure P_{ei} in the transmissivity of equation (9) allows the total band absorbance to be determined for each gas band. When two or more gases have bands in the same spectral interval, an overlap correction must be introduced. With equation (8), the total band absorbances, and the overlap correction must be introduced. Data for using Edwards exponential wide band model taken from [3] are shown in Table 1. Variations of this model are given in [7].

As mentioned, narrow band radiation data and models for combustion gases are also available. The SRRM [8] data base is build on empirical data taken with modest spectral resolution. The experiments were conducted primarily at atmospheric and sub-atmospheric pressure to evaluate rocket plume radiation. Recently, studies have been made to model molecular radiation directly by modeling all of the lines in a band. This has resulted in the HITRAN data base [9-12]. Phillips [9] made a comparison between the band predictions using the SRRM and HITRAN data; his work is still in progress. Several investigators have used the individual line data to predict and measure radiation at high pressures and modestly high temperatures (about 800 °K) [13-16]. Such data are very interesting to compare to wide band predictions, but require too much computational time to be utilized directly for simulating combustor heating. Leckner [17] compares integrations of narrow band model data for H₂O and CO₂ to mean absorption coefficient measurements.

To account for soot radiation, a medium containing only particles may be considered. Small particles present in a medium attenuate radiation continuously throughout the spectrum. For small particle absorption, of any size distribution, the governing equation for the absorption coefficient is given as [1, 8]

$$k_{rp} = \frac{3}{2} \frac{Q_{abs}}{2r} f_v = \frac{36\pi f_v}{\lambda} \frac{nk}{[n^2 - k^2 + 2]^2 + (2nk)^2} \quad (10)$$

where k_{rp} is the particle absorption coefficient, r the particle radius, Q_{abs} the absorption efficiency, f_v the volume fraction of particles, and $m = n - ik$ the index of refraction. The actual wavelength variation indicated in equation (10) is dependent upon the variation of m for the specific particles. For soot particles that are contained in combustion systems, the optical

Table 1. Wide band model correlation parameters for various gases						
Band Location		Pressure Parameters		Correlation Parameters		
λ [μm]	(δ_k)	n	b	α_0 [$\text{cm}^{-1}/(\text{g}/\text{m}^2)$]	γ_0	ω_0 [cm^{-1}]
H₂O $m = 3$, $\eta_1 = 3652 \text{ cm}^{-1}$, $\eta_2 = 1595 \text{ cm}^{-1}$, $\eta_3 = 3756 \text{ cm}^{-1}$, $g_k = (1, 1, 1)$						
71 μm^a	$\eta_c = 140 \text{ cm}^{-1}$ (Rotational) (0,0,0)	1	$8.6 (T_0/T)^{0.5} + 0.5$	44,205	0.14311	69.3
6.3 μm	$\eta_c = 1600 \text{ cm}^{-1}$ (0,1,0)	1	$8.6 (T_0/T)^{0.5} + 0.5$	41.2	0.09427	56.4
2.7 μm	$\eta_c = 3760 \text{ cm}^{-1}$ (0,2,0) (1,0,0) (0,0,1)	1	$8.6 (T_0/T)^{0.5} + 0.5$	0.2 2.3 23.4	0.13219 ^{b,c}	60.0 ^b
1.87 μm	$\eta_c = 5350 \text{ cm}^{-1}$ (0,1,1)	1	$8.6 (T_0/T)^{0.5} + 1.5$	3.0	0.08169	43.1
1.38 μm	$\eta_c = 7250 \text{ cm}^{-1}$ (1,0,1)	1	$8.6 (T_0/T)^{0.5} + 1.5$	2.5	0.11628	32.0
CO₂ $m = 3$, $\eta_1 = 1351 \text{ cm}^{-1}$, $\eta_2 = 666 \text{ cm}^{-1}$, $\eta_3 = 2396 \text{ cm}^{-1}$, $g_k = (1, 2, 1)$						
15 μm	$\eta_c = 667 \text{ cm}^{-1}$ (0,1,0)	0.7	1.3	19.0	0.06157	12.7
10.4 μm	$\eta_c = 960 \text{ cm}^{-1}$ (-1,0,1)	0.8	1.3	2.47×10^{-9}	0.04017	13.4
9.4 μm	$\eta_c = 1060 \text{ cm}^{-1}$ (0,-2,1)	0.8	1.3	2.48×10^{-9}	0.11888	10.1
4.3 μm	$\eta_c = 2410 \text{ cm}^{-1}$ (0,0,1)	0.8	1.3	110.0	0.24723	11.2
2.7 μm	$\eta_c = 3660 \text{ cm}^{-1}$ (1,0,1)	0.65	1.3	4.0	0.13341	23.5
2.0 μm	$\eta_c = 5200 \text{ cm}^{-1}$ (2,0,1)	0.65	1.3	0.060	0.39305	34.5
CO $m = 1$, $\eta_1 = 2143 \text{ cm}^{-1}$, $g_1 = 1$						
4.7 μm	$\eta_c = 2143 \text{ cm}^{-1}$ (1)	0.8	1.1	20.9	0.07506	25.5
2.35 μm	$\eta_c = 4260 \text{ cm}^{-1}$ (2)	0.8	1.0	0.14	0.16758	20.0

Footnotes for Table 1. Parameters for the EWB Model

- a. For the rotational band $\alpha = \alpha_0 \exp(-9 (T_0/T)^{0.5})$, $\gamma = \gamma_0 (T_0/T)^{0.5}$
- b. Combination of three bands, all but weak (0,2,0) band are fundamental bands, $\alpha_0 = 25.9 \text{ cm}^{-1}$
- c. Line overlap for overlapping bands from

$$\alpha = \alpha_0 \frac{\Psi^*}{\Psi_0^*}, \quad \omega = \omega_0 \sqrt{\frac{T}{T_0}}, \quad \beta = \gamma P_e = \gamma_0 \sqrt{\frac{T_0}{T}} \frac{\phi}{\phi_0} P_e, \quad P_e = \left[\frac{p}{p_0} (1 + (b-1) \frac{p_a}{p}) \right]^n$$

$$T_0 = 100^\circ\text{K}, \quad p_0 = 1 \text{ atm}$$

$$\alpha(T) = \alpha_0 \frac{\Psi^*(T)}{\Psi^*(T_0)} = \alpha_0 \frac{\left\{ 1 - \exp \left(- \sum_{k=1}^m u_k \delta_k \right) \right\} \Psi(T)}{\left\{ 1 - \exp \left(- \sum_{k=1}^m u_{0,k} \delta_k \right) \right\} \Psi(T_0)}$$

$$\Psi(T) = \frac{\prod_{k=1}^m \sum_{v_k=v_{0,k}}^{\infty} \frac{(v_k + g_k + \delta_k - 1)!}{(g_k - 1)! v_k!} e^{-u_k v_k}}{\prod_{k=1}^m \sum_{v_k=0}^{\infty} \frac{(v_k + g_k - 1)!}{(g_k - 1)! v_k!} e^{-u_k v_k}}$$

$$\Phi(T) = \frac{\left\{ \prod_{k=1}^m \sum_{v_k=v_{0,k}}^{\infty} \sqrt{\frac{(v_k + g_k + \delta_k - 1)!}{(g_k - 1)! v_k!}} e^{-u_k v_k} \right\}^2}{\prod_{k=1}^m \sum_{v_k=0}^{\infty} \frac{(v_k + g_k + \delta_k - 1)!}{(g_k - 1)! v_k!} e^{-u_k v_k}}$$

$$A^* = A/\omega$$

$$\tau_0 = \alpha X/\omega$$

$$A^* = \tau_0$$

$$A^* = 2(\tau_0 \beta)^{0.5} - \beta$$

$$A^* = \ln \{ \tau_0 \beta \} + 2 - \beta$$

$$A^* = \tau_0$$

$$A^* = \ln \tau_0 + 1$$

$$X = \text{distance}$$

$$\text{for } \beta \leq 1 \text{ and } 0 \leq \tau_0 \leq \beta$$

$$\text{for } \beta \leq 1 \text{ and } \beta \leq \tau_0 \leq 1/\beta$$

$$\text{for } \beta \leq 1 \text{ and } 1/\beta \leq \tau_0 \leq \infty$$

$$\text{for } \beta \leq 1 \text{ and } 0 \leq \tau_0 \leq 1$$

$$\text{for } \beta \leq 1 \text{ and } 1 \leq \tau_0 \leq \infty$$

properties have been recently reviewed by Reid [18]. The review indicated that several dispersion models for m have been reported. Furthermore, although the dispersion models indicate significant differences in m the predicted volume IR absorption coefficients vary much less. These investigators chose the model of Lee and Tien [19] for coding to generate Figure 1. These index of refraction values are recommended until better data become available. The data are believed to be reasonably accurate.

Using this radiation model for soot, the rocket motor test data of Boynton [20] were re-analyzed. The soot density was determined by considering the soot to be the sole radiator at $2.2 \mu\text{m}$. The re-analyzed data are shown in Figs. 2-4 for three nozzle configurations. The excellent fits of the test data show that the results are consistent with the Lee & Tien radiation model. The test report suggested that gaseous radiation was estimated and removed from the particle radiation, but details of this removal process were not specified. Additional analyses of these data are presented in the Phase II progress reports [21] that this Phase III study supports.

Using equation (9) in the transmissivity given in equation (3) results in

$$\tau_{rp}\{s\} = \exp \left[-\frac{3}{2} \frac{Q_{abs}}{2r} \int_0^s f_s ds' \right] \quad (11)$$

For a homogeneous path, f_s is a constant and the integral in equation (11) is $f_s s$. This result gives the intensity for a particulate medium in terms of the particle's properties, temperature, and pathlength. This can also be used to determine the temperature of the homogeneous path if f_s , Q_{abs} , and L are known.

If the medium is composed of both particles and gases, the overlapping spectra must be analyzed. Particulate emission and absorption is continuous and is essentially constant over the banded gas regions. Therefore, the particle transmissivity can be removed from integrals over gas bands and evaluated at the band center or head. The governing equation for the total intensity is

$$I^{-}\{0\} = \int_0^x I_{br} (1 - \tau_{rp}) d\nu + \sum_{ij} \overline{\tau_{rp}}_{ij} I_{brij} A_{ij} \quad (12)$$

where A_{ij} accounts for the overlap of species with one another and τ_{rp} is the transmissivity of the particles. The first term denotes the intensity resulting from particulates, and the second term denotes the gaseous contribution that is transmitted through the particles. This is the result for the intensity leaving a homogeneous path containing gases and particles. The applicability of this result is dependent upon the degree of homogeneity present in the system.

Edwards [22] presented results of this type simulation for conditions typical of a rocket motor with pressure level as a parameter. The highest pressure which he considered was about 950 psi. At this pressure the radiation is still not blackbody (for the soot level which was

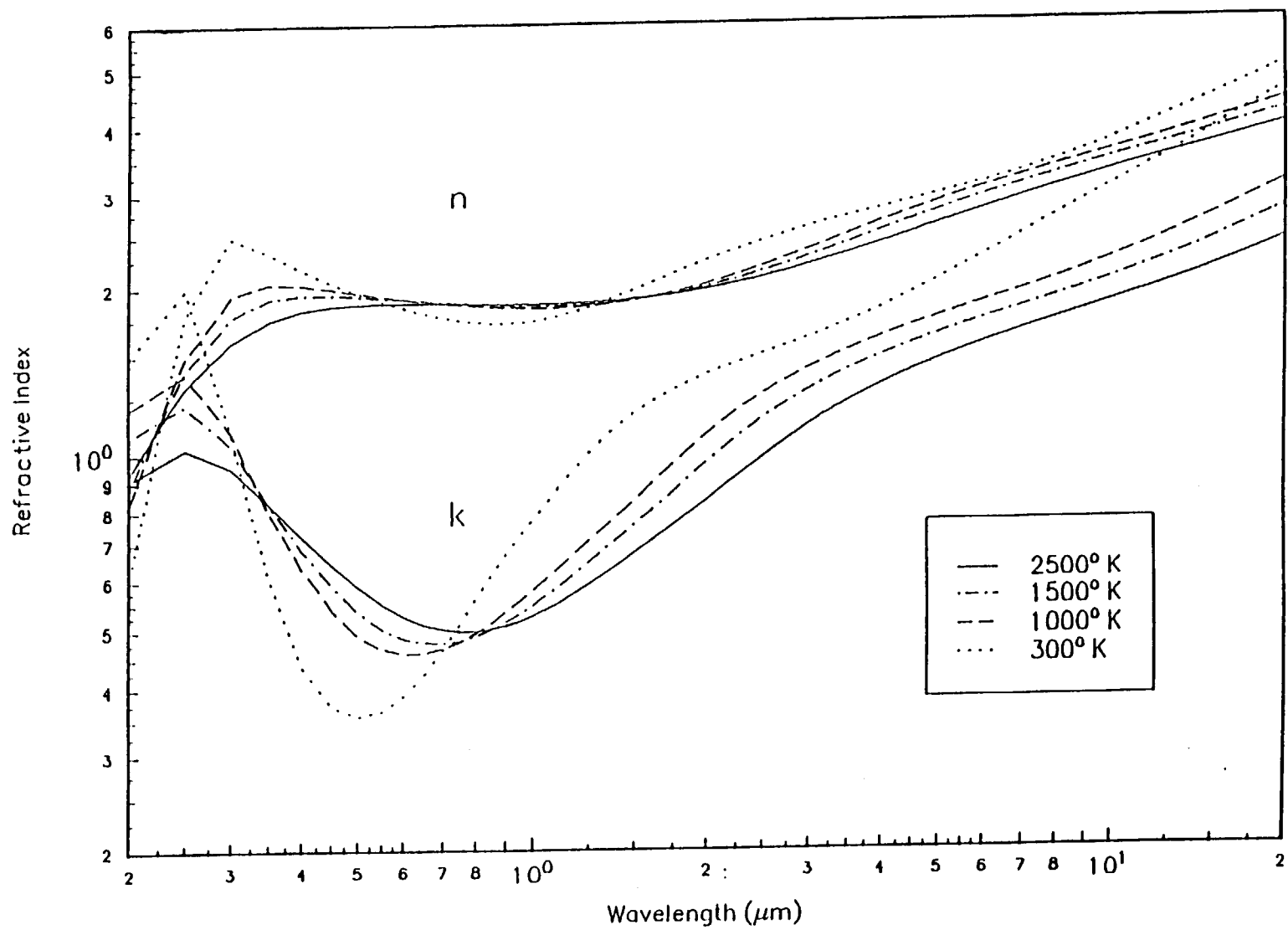


Figure 1. Optical Properties for Soot

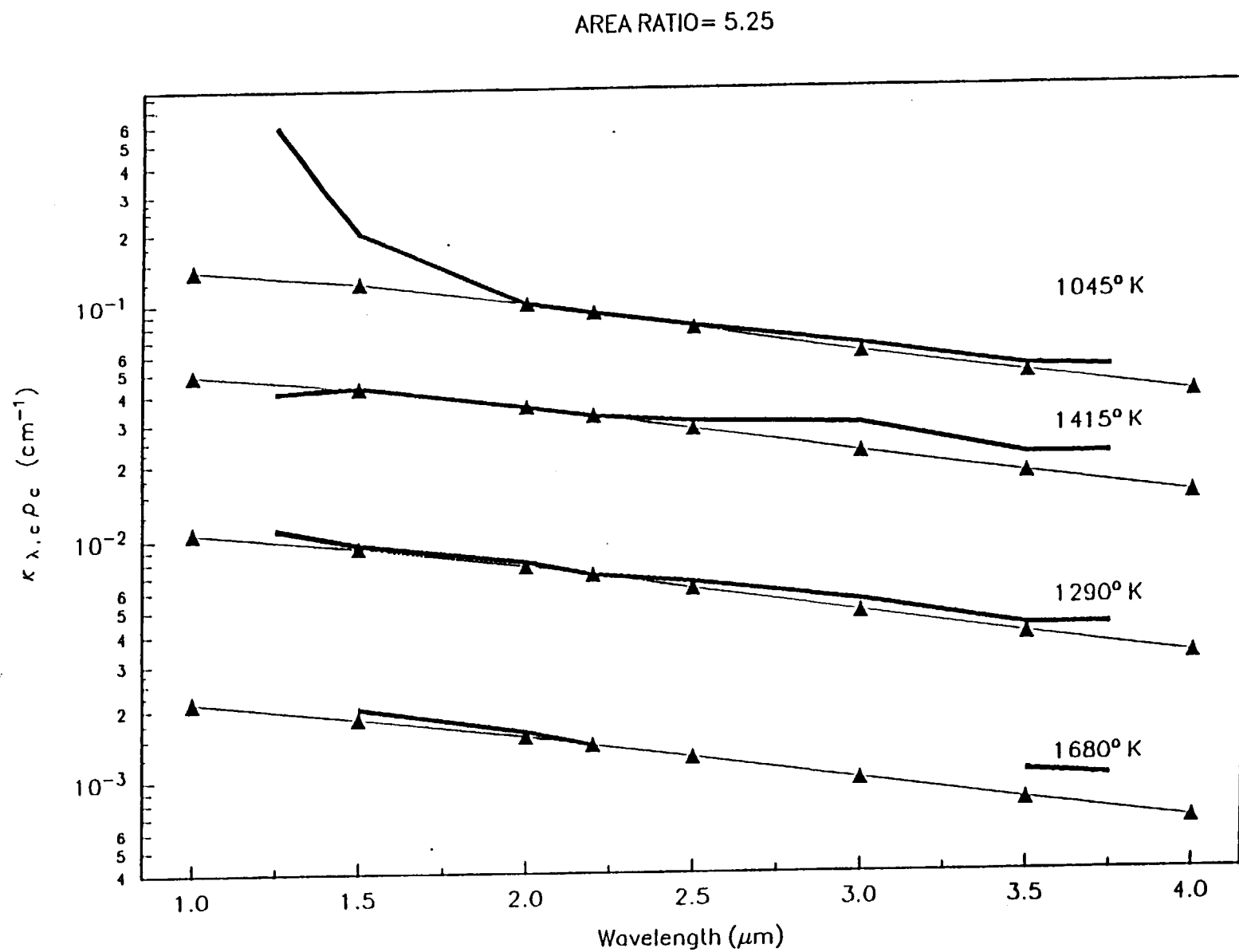


Figure 2.14 Foelsch Nozzle Radiation Measurements - High Expansion Ratio

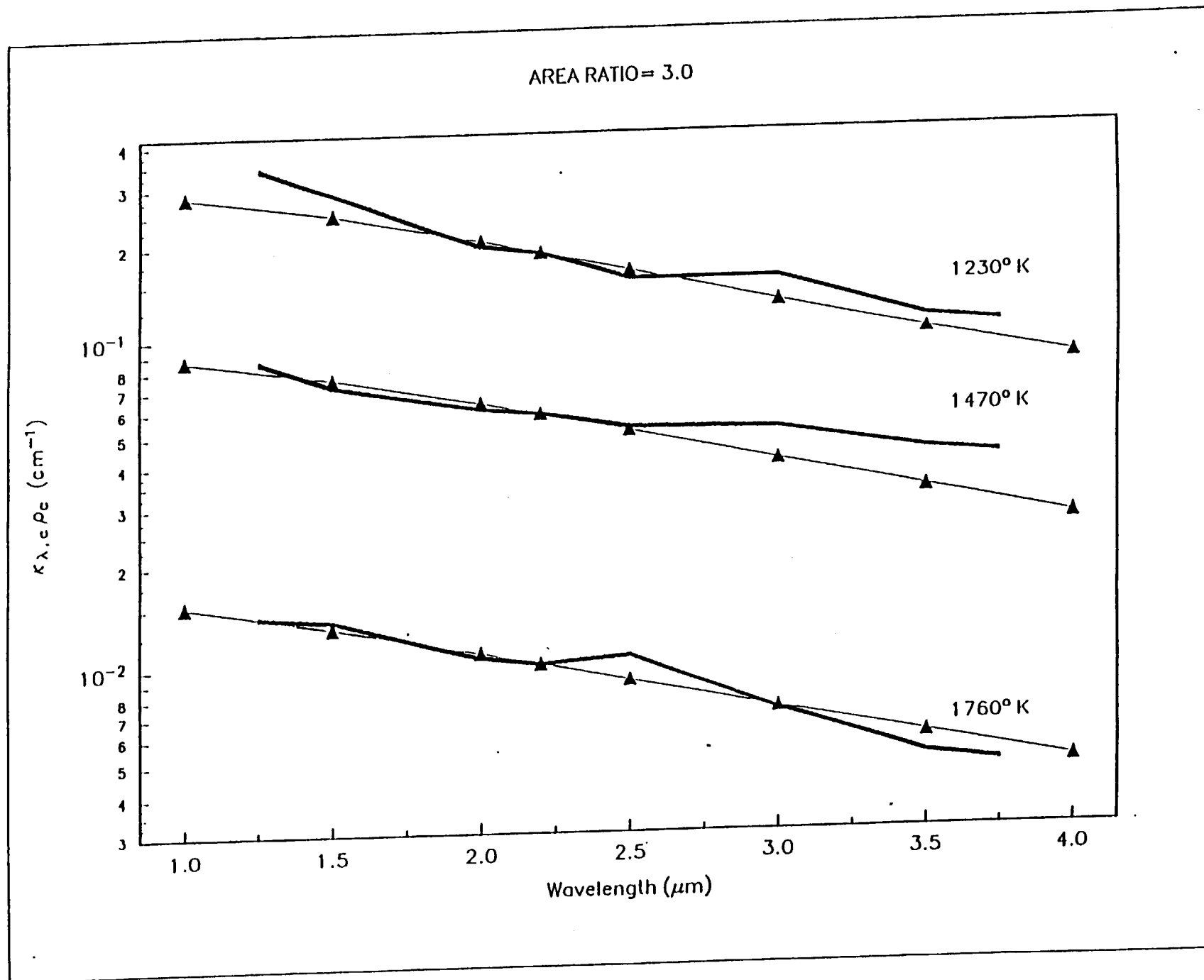


Figure 3. Foelsch Nozzle Radiation Measurements - Medium Expansion Ratio

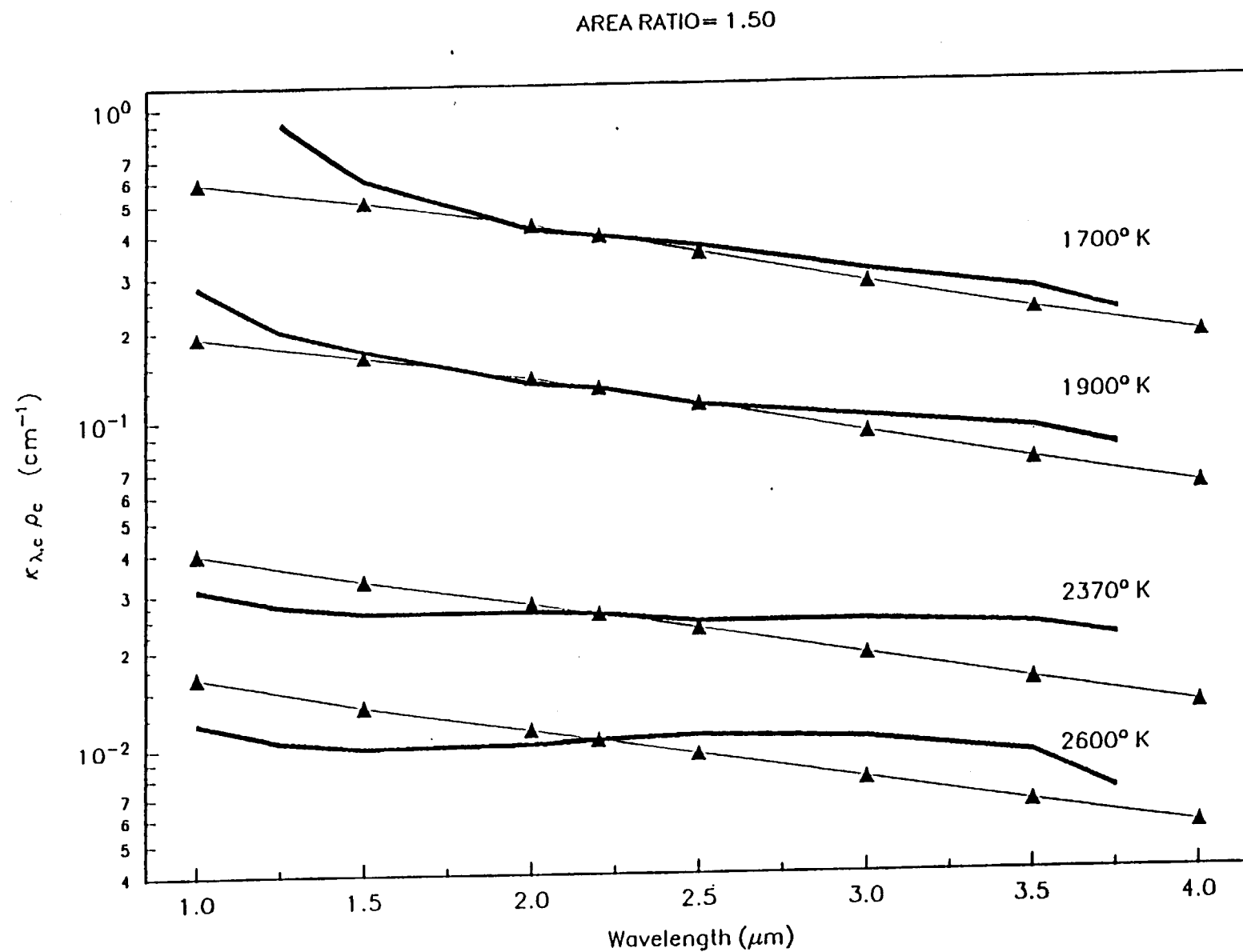


Figure 4. Foelsch Nozzle Radiation Measurements - Low Expansion Ratio

assumed). This result is shown in Fig. 5, and it suggests that his radiation property estimation method might be useful for predicting radiation within rocket combustors. Had blackbody radiation been predicted at this and lower pressures, the method would have been suspect and further consideration been recommended.

- Non-homogeneous nongray model

The most complete method to determine the intensity from a general pathlength is to incorporate the variations in temperature and pressure. The analysis needed is, therefore, more complicated, and more detailed information is required. The resulting expressions are used for pathlengths that have large variations in temperature and pressure where the homogeneous nongray model is no longer valid.

The general non-homogeneous intensity at $s = 0$ is given in equation (5). Similar to equation (12) for a homogeneous nongray path, the non-homogeneous nongray model for a mixture of particles and gases is given as

$$I^{-}\{0\} = \int_0^{\infty} \int_0^L I_{bv} \frac{d}{ds} [1 - \tau_{vp}\{s\}] ds dv + \int_0^L \overline{I_{bv}} \frac{d}{ds} \left\{ \tau_p\{s\} \int_0^s [1 - \tau_{vg}\{s'\}] dv \right\} ds \quad (13)$$

$$I^{-}\{0\} = \int_0^{\infty} \int_0^L I_{bv} \frac{d}{ds} [1 - \tau_{vp}\{s\}] ds dv + \int_0^L \sum_{ij} \overline{I_{bvij}} \frac{d}{ds} [\overline{\tau_{vpj}} A_{ij}] ds \quad (14)$$

where the overlap correction is introduced into A_{ij} . The terms of equation (14) are interpreted in a similar manner to the homogeneous result equation (12) except that all quantities are now pathlength dependent. This is the general governing expression for the non-homogeneous nongray model.

An approximate method of averaging to replace non-homogeneous regions with scaled values of the wide band parameters for use in the homogeneous total band absorptance has been reported [23]. This work gives the average values as

$$\overline{\sigma} = \frac{1}{s} \int_0^s \sigma ds' \quad (15)$$

The use of any of the scaling techniques requires detailed pathlength information about the variation of the partial pressure and temperature.

- Solution of the Uncoupled Radiative Transfer Equation

The radiative transfer equation (RTE) is an integro-differential equation that expresses

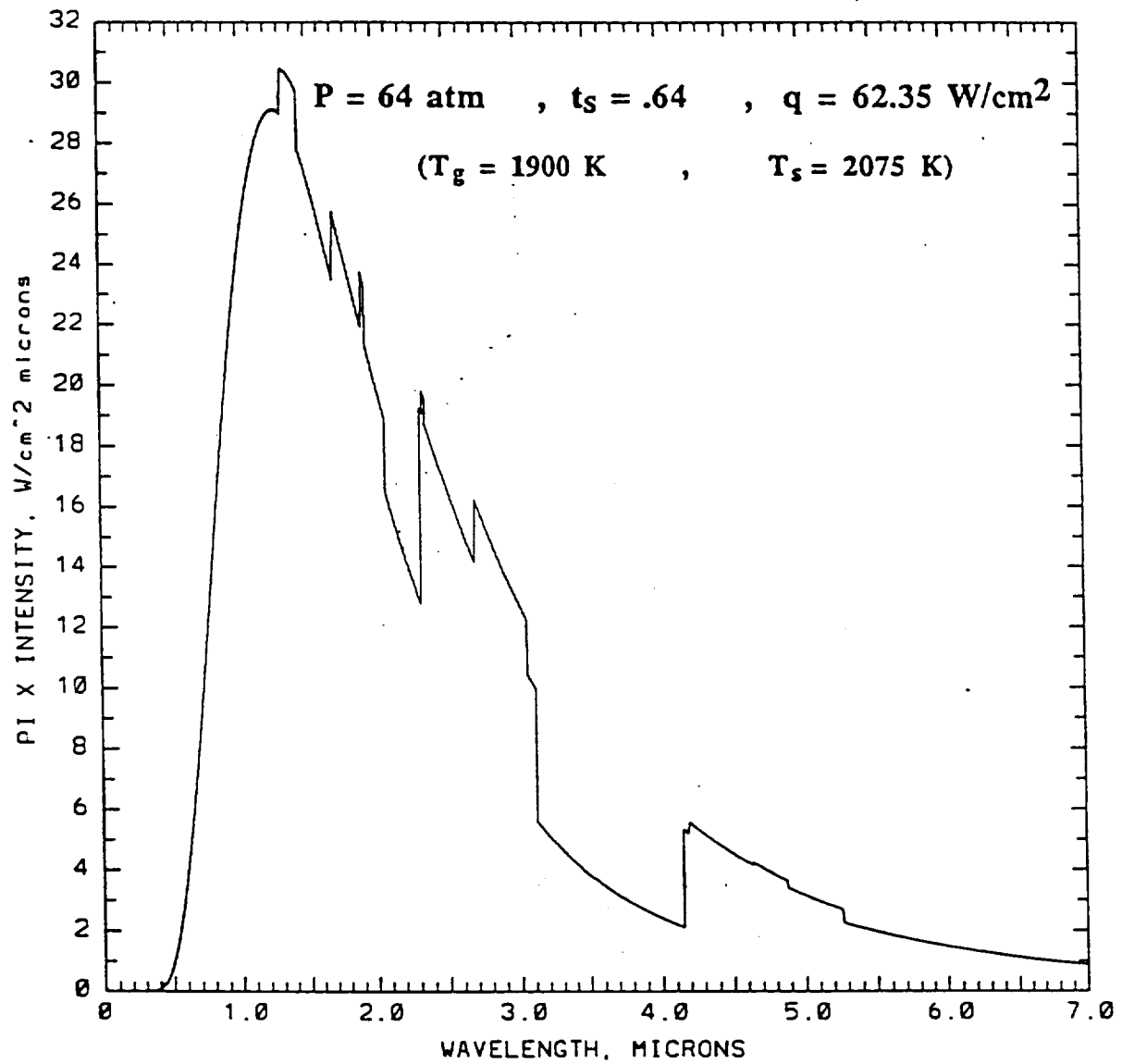


Figure 5. Combustion Gas and Soot Radiation

the conservation of radiation. The concentration and temperature fields are needed to evaluate this equation. From a solution of the RTE a radiation heat flux vector (q_r) can be obtained which enters directly into the energy equation. Usually q_r is small enough that it can be neglected in the energy equation, such that the RTE can be solved in an uncoupled fashion after the remaining conservation equations are solved. This is most fortunate, because the RTE cannot be solved in general, even numerically. The closest approach is to use a Monte Carlo [24] simulation to obtain the RTE solution. It is not feasible to obtain a Monte Carlo solution at each grid point at each CFD time step to generate a truly coupled solution of the entire system of conservation equations. This dilemma has resulted in a multitude of approximate RTE solutions being used to represent the radiation in the expectation that some form of "coupled" solution can be obtained. It is absolutely essential that realistic line-of-sight (LOS) radiance calculations be made in order to determine the extent to which approximations can be accepted in RTE solutions. The radiation properties presented in the previous section are sufficiently accurate to make the LOS analyses using the RTE solution technology described in the following paragraph. The critical issue is the accuracy of the prediction of gaseous species and soot concentrations which characterize tripropellant combustor flowfields of interest.

SECA has developed and/or collected and utilized several codes for use in predicting radiation. These codes are listed and described in Table 2. The Lee and Tien soot data are indicated as L&T soot in Table 2. The NOZZRAD [25], GASRAD [26], and SRRM [8] codes are particularly suitable for evaluating LOS radiance characteristics. The NOZZRAD code can be used as a subroutine to provide LOS data for use in other radiation analyses such as IDA [27]. The IDA code is best method of offering a fully coupled radiation analysis, provided the LOS analyses justify the assumptions used in its development. The diffusion approximation code (DAC) [27] offers a very convenient method of predicting wall heating, again provided its use can be justified.

The LOS analyses were planned as part of this study, but the reduced effort resulting from funding limitations and the fact that all of the other aspects of the study had to be performed first in order to obtain realistic concentration fields (especially of soot) prevented these analyses from being made. Upstream radiative heating of the flowfield near the injector face and of the injector face itself is extremely important for rocket motor design, but these flowfields are very difficult to predict due to geometrical complexity and the possible presence of significant amounts of liquid droplets. Hence, their prediction is a costly and uncertain endeavor.

● Coupled Radiative Transfer Equation Solutions

The extensive furnace modeling efforts of Lockwood and his colleagues [28] and flame modeling studies at the Naval Research Laboratory [29] and by Moss, et al [30] indicate that CFD/radiation analyses are feasible. However, none of these studies simulated conditions which are typical of rocket motor combustion, and all of the radiation analyses contain approximations which must be re-examined before they can be applied to rocket motor combustion chambers. The flame studies performed at the National Research Council of Canada [31] are very valuable for verifying concentration predictions of tripropellant combustion since hydrogen enriched hydrocarbon flames were investigated by radiation experiments using a CARS system.

Table 2. RTE Solvers				
Code	Methodology	Geometry for Non-Homogeneous Fields	Optical Properties	Ref.
NOZZRAD	emission /absorption/ scattering	i. LOS ii. Slabs	L&T soot/ Al_2O_3 particles wide band model	25
SIRRM	emission/absorption/ scattering	i. LOS ii. 2-& 6 Flux	old soot data, Al_2O_3 , narrow band model	8
GASRAD	emission/absorption	LOS from cylindrical field	old soot data, narrow band model	26
IDA	emission/absorption/ scattering w/ordinary differential approximation	Cylindrical coordinates	Al_2O_3 , wide band model	27
DAC	emission/absorption/ scattering diffusion limit	Cylindrical coordinates	Al_2O_3 L&T soot, wide band model	27
REMCAR	emission/absorption/ scattering, Monte Carlo	3-dimensional	Al_2O_3 , old soot data, narrow band model	24

Nomenclature for Appendix A

A_{ij}	total band absorptance for jth band of the ith species
\bar{c}	concentration of particles
C_2	Planck's second constant
f_v	volume fraction of soot particles
I	intensity
I^-	intensity in the negative s direction
k	complex part of refractive index
k_v	absorption coefficient
K	average absorption coefficient
L	pathlength
m	complex index of refraction equal to $n-ik$
n	real part of refractive index
P	pressure
P_{ei}	equivalent broadening pressure of the ith species
Q_{abs}	particle absorption efficiency
r	particle radius
s	distance along line of sight
T	temperature
X	mass pathlength

Greek symbols

α_{ij}	integrated band intensity
β_{ij}	π times the mean line width-to-spacing ratio
ϵ	emissivity
λ	wavelength
ν	wave number
ρ	solid phase density of soot
ρ_i	density of ith absorber
τ	transmissivity
ω_{ij}	band width parameter

Subscripts

b	blackbody
i	species
j	band of specific species
l	lower wave number limit
p	particle
sc	scaled parameter
u	upper wave number limit
ν	wave number

Superscripts

$\bar{}$	(overbars) average values
$\{ \}$	denote functionality

References for Appendix A

1. Buckius, R.O., and C.L. Tien, "Infrared Flame Radiation," Int. J. Heat Mass Transfer, **20**, pp. 93-106, Pergamon Press, 1977.
2. Goody, R.M., Atmospheric Radiation, Theoretical Basis, I, Oxford University Press, 1964.
3. Modest, M.F., Radiative Heat Transfer, McGraw-Hill, New York, 1993.
4. Edwards, D.K., "Molecular Gas Band Radiation," Irvine, T.F., Jr., and J. P. Hartnett Eds., Advances in Heat Transfer, **12**, pp. 115-193, Academic Press, New York, 1976.
5. Ludwig, C.B., W. Malkmus, J.E. Reardon, and J.A.L. Thompson, "Handbook of Infrared Radiation From Combustion Gases," NASA/MSFC, NASA SP-3080, 1973.
6. Edwards, D.K., Radiation Heat Transfer Notes, Hemisphere Publishing Corporation, 1981.
7. Felske, J.D., and C.L. Tien, "Wide Band Characterization of the Total Band Absorptance of Overlapping Infrared Gas Bands," Combustion Science and Technology, **11**, pp. 111-117, Gordon and Bready, Science Publishers Ltd., The United Kingdom, 1975
8. Markarian, P., and R. Kosson, "Standardized Infrared Radiation Model (SIRRM-II)," AFAL-87-098, Grumman Aerospace Corp., Bethpage, NY, March, 1988.
9. Phillips, W.J., "Band Model Parameters For H₂O and CO₂ in the 300-1,000 K Temperature Region," AIAA-91-1429, AIAA 26th Thermophysics Conference, Honolulu, Hawaii, June 1991.
10. Brodbeck, C., et al, "Absorption of Radiation by Gases from Low to High Pressures. II. Measurements and Calculations of CO Infrared Spectra," Journal de Physique II, France, pp. 2101-2118, December 1994.
11. Hartmann, J.M., et al, "Line-By-Line and Narrow-Band Statistical Model Calculations for H₂O," J. Quant. Spectrosc. Radiat. Transfer, **12**, pp. 119-127, Pergamon Press, Ltd., 1984.
12. Hartmann, J.J., "Absorption of Radiation by Gases from Low to High Pressures. I. Empirical Line-By-Line and Narrow-Band Statistical Models," Journal de Physique II, France, pp. 739-762, April 1991.
13. Sougiani, A., J.M. Hartman, and J. Taine, "Validity of Band-Model Calculations for CO₂ and H₂O Applied to Radiative Properties and Conductive-Radiative Transfer," J. Quant. Spectrosc. Radiat. Transfer, **33**, pp. 243-257, Pergamon Press, Ltd., 1985.
14. Thomas, M. E., "Infrared- And Millimeter-Wavelength Continuum Absorption in the Atmospheric Windows: Measurements and Models," Infrared Phys., **30**, pp. 161-174, Pergamon Press, 1990.
15. Perrin, M.Y., and J.M. Hartmann, "Temperature-Dependent Measurements and Modeling of Absorption by CO₂-N₂ Mixtures in the Far Line-Wings of the 4.3 μ m CO₂ Band," J. Quant. Spectrosc. Radiat. Transfer, **33**, pp. 311-317, Pergamon Press, Ltd., 1989.
16. Hartmann, J.M., et al, "The Infrared Continuum of Pure Water Vapor: Calculations and High-Temperature Measurements," J. Quant. Spectrosc. Radiat. Transfer, **49**, pp. 675-691, Pergamon Press, Ltd., 1993.
17. Leckner, B., "Spectral and Total Emissivity of Water Vapor and Carbon Dioxide," Combustion and Flame, **19**, pp. 33-48, 1972.

18. Reed, Bob, AEDC, Sverdrup Technology, Memorandum, "Optical Properties of Soot for Signature Prediction", 15 November 1993.
19. Lee, S.C., and C. L. Tien, "Optical Constants of Soot in Hydrocarbon Flames," Eighteenth Symposium (Int) on Combustion, The Combustion Institute, p. p. 1159-1166, 1981.
20. Boynton, F.P., "Study on the Spectral Emissivity of Carbon Particles Produced by a Rocket Motor," General Dynamics/Convair Report GD/C-DBE66-006, May, 1966.
21. Farmer, R.C., P.G. Anderson, and G.C. Cheng, Progress Reports on "Propulsion Chemistry for CFD Applications, under NAS8-40574, SECA, Inc., Huntsville, AL, ongoing.
22. JANNAF Workshop Summary, "Radiation Effects on Flow Characteristics in Combustion Chambers," Monterey, CA, July 1989.
23. Felske, J.D. and C.L. Tien, "Infrared Radiation From Non-Homogeneous Gas Mixtures Having Overlapping Bands," J. Quant. Spectrosc. Radiat. Transfer, 14, Pergamon Press, Great Britain, pp. 35-48, 1974.
24. Everson, J., and H. F. Nelson, "Development and Application of a Reverse Monte Carlo Radiative Transfer Code for Rocket Plume Base Heating," AIAA 93-0138, 31st Aerospace Sciences Meeting, Reno, NV, January 1993.
25. Farmer, R.C., et al, "Radiation From Advanced Solid Rocket Motor Plumes," SECA-FR-94-18, SECA, Inc., Huntsville, AL, December 1994.
26. Reardon, J.E., and Y.C. Lee, "A Computer Program for Thermal Radiation from Gaseous Rocket Exhaust Plumes (GASRAD)," RTR 014-9, Remtech, Inc., Huntsville, AL, December 1979.
27. Saladino, A.J., and R.C. Farmer, "Radiation/Convection Coupling in Rocket Motor & Plume Analysis," SECA-FR-93-10, SECA, Inc., Huntsville, AL, July 1993.
28. Lockwood, F.C., and B. Shen, "Performance Predictions of Pulverized-Coal Flames of Power Station Furnace and Cement Kiln Types," Twenty-Fifth Symposium (Int) on Combustion, The Combustion Institute, pp. 503-509, 1994.
29. Kaplan, C.R., S.W. Baek, E.S. Oran and J.L. Ellzey, "Dynamics of a Strongly Radiating Unsteady Ethylene Jet Diffusion Flame," Manuscript prepared for submission to Combustion and Flame.
30. Bressloff, N.W., J.B. Moss and P.A. Rubini, "CFD Prediction of Coupled Radiation Heat Transfer and Soot Production in Turbulent Flames," Twenty-Sixth Symposium (Int) on Combustion, The Combustion Institute, pp. 2379-2386, 1996.
31. Gulder, O.L., D.R. Snelling and R.A. Sawchuk, "Influence of Hydrogen Addition to Fuel on Temperature Field and Soot Formation in Diffusion Flames," Twenty-Sixth Symposium (Int) on Combustion, The Combustion Institute, pp. 2351-2358, 1996.

REPORT DOCUMENTATION PAGE

Form Approved
OMB No. 0704-0188

Public reporting burden for this collection of information is estimated to average 1 hour per response, including the time for reviewing instructions, searching existing data sources, gathering and maintaining the data needed, and completing and reviewing the collection of information. Send comments regarding this burden estimate or any other aspect of this collection of information, including suggestions for reducing this burden, to Washington Headquarters Services, Directorate for Information Operations and Reports, 1215 Jefferson Davis Highway, Suite 1204, Arlington, VA 22202-4302, and to the Office of Management and Budget, Paperwork Reduction Project (0704-0188), Washington, DC 20503.

1. AGENCY USE ONLY (Leave blank)		2. REPORT DATE May, 1997		3. REPORT TYPE AND DATES COVERED Final Report - April 95/97	
4. TITLE AND SUBTITLE DEVELOPMENT OF TRIPROPELLANT CFD DESIGN CODE				5. FUNDING NUMBERS NAS8-40583	
6. AUTHOR(S) Richard C. Farmer Gary C. Cheng Peter G. Anderson					
7. PERFORMING ORGANIZATION NAME(S) AND ADDRESS(ES) SECA, Inc. 3313 Bob Wallace Avenue, Suite 202 Huntsville, AL 35805				8. PERFORMING ORGANIZATION REPORT NUMBER SECA-FR-97-04	
9. SPONSORING / MONITORING AGENCY NAME(S) AND ADDRESS(ES) NASA/MSFC Marshall Space Flight Center, AL 35812				10. SPONSORING / MONITORING AGENCY REPORT NUMBER	
11. SUPPLEMENTARY NOTES					
12a. DISTRIBUTION / AVAILABILITY STATEMENT				12b. DISTRIBUTION CODE	
13. ABSTRACT (Maximum 200 words) A tripropellant, such as $GO_2/H_2/RP-1$, CFD design code has been developed to predict the local mixing of multiple propellant streams as they are injected into a rocket motor. The code utilizes real fluid properties to account for the mixing and finite-rate combustion processes which occur near an injector faceplate, thus the analysis serves as a multi-phase homogeneous spray combustion model. Proper accounting of the combustion allows accurate gas-side temperature predictions which are essential for accurate wall heating analyses. The complex secondary flows which are predicted to occur near a faceplate cannot be quantitatively predicted by less accurate methodology. Test cases have been simulated to describe an axisymmetric tripropellant coaxial injector and a 3-dimensional $RP-1/LO_2$ impinger injector system. The analysis has been shown to realistically describe such injector combustion flowfields. The code is also valuable to design meaningful future experiments by determining the critical location and type of measurements needed.					
14. SUBJECT TERMS				15. NUMBER OF PAGES 58	
				16. PRICE CODE	
17. SECURITY CLASSIFICATION OF REPORT unclassified	18. SECURITY CLASSIFICATION OF THIS PAGE unclassified	19. SECURITY CLASSIFICATION OF ABSTRACT unclassified	20. LIMITATION OF ABSTRACT UL		